

2

AD-A244 783



**Technical Report
931**

**Compensating for Groundplane
Deformations of a Space-Based Radar to
Improve Clutter Cancellation Performance**

**DTIC
ELECTE
JAN 21 1992
S B D**

G.H. Emmons

92-01596



5 November 1991

Lincoln Laboratory

MASSACHUSETTS INSTITUTE OF TECHNOLOGY

LEXINGTON, MASSACHUSETTS



Prepared for the Department of the Air Force
under Contract F19628-90-C-0002.

Approved for public release; distribution is unlimited.

92 1 17 02

This report is based on studies performed at Lincoln Laboratory, a center for research operated by Massachusetts Institute of Technology. The work was sponsored by the Department of the Air Force under Contract F19628-90-C-0002.

This report may be reproduced to satisfy needs of U.S. Government agencies.

The ESD Public Affairs Office has reviewed this report, and it is releasable to the National Technical Information Service, where it will be available to the general public, including foreign nationals.

This technical report has been reviewed and is approved for publication.

FOR THE COMMANDER

Hugh L. Southall

Hugh L. Southall, Lt. Col., USAF
Chief, ESD Lincoln Laboratory Project Office

Non-Lincoln Recipients

PLEASE DO NOT RETURN

Permission is given to destroy this document
when it is no longer needed.

MASSACHUSETTS INSTITUTE OF TECHNOLOGY
LINCOLN LABORATORY

**COMPENSATING FOR GROUNDPLANE
DEFORMATIONS OF A SPACE-BASED RADAR TO
IMPROVE CLUTTER CANCELLATION PERFORMANCE**

G.H. EMMONS
Group 61

TECHNICAL REPORT 931

5 NOVEMBER 1991

Approved for public release; distribution is unlimited.

LEXINGTON

MASSACHUSETTS

ABSTRACT

Effects of deformations on the clutter cancellation of a hypothetical large phased-array space-based radar antenna groundplane are described. The radar is assumed to use a displaced-phase-center antenna (DPCA) for cancelling stationary ground clutter. A multilateration method of measuring the deformations is analyzed to determine its effectiveness in compensating for the deformations and improving clutter cancellation. Finally, a data staleness problem inherent in the proposed serial sampling method is described, a potential solution is presented, and its feasibility is discussed.



Accession For	
NTIS GRA&I	<input checked="checked" type="checkbox"/>
DTIC TAB	<input type="checkbox"/>
Unannounced	<input type="checkbox"/>
Justification	
By	
Distribution/	
Availability Codes	
Dist	Avail and/or Special
A-1	

TABLE OF CONTENTS

Abstract	iii
List of Illustrations	vii
List of Tables	xi
1. INTRODUCTION	1
1.1 Trade-Offs	1
1.2 Previously Proposed Methods of Compensating for Deformations	2
1.3 Outline of Report	3
2. OBJECTIVES	5
2.1 SBR Antenna Model	5
2.2 Algorithm for Steering the Antenna	5
2.3 Clutter Cancellation	5
2.4 Groundplane Deformation Model	7
2.5 Effects of Uncompensated Deformations of Clutter Cancellation	15
2.6 Estimating Deformations—Multilateration	18
2.7 Results: Static Deformation	22
2.8 Results: Dynamic Deformation	29
2.9 Timeline Problems for Vibrations	32
2.10 Serial Measurements and Prediction	33
2.11 Prediction Results	38
3. SUMMARY, CRITIQUE, AND UNFINISHED WORK	43
APPENDIX A. CLUTTER CANCELLATION	45
APPENDIX B. DEFORMATIONS	47
APPENDIX C. MULTILATERATION	53
APPENDIX D. LEAST SQUARES	57
REFERENCES	59

LIST OF ILLUSTRATIONS

Figure No.		Page
1	Conceptual design for a large space-based radar.	2
2	Radar antenna used to investigate effects of deformation.	6
3	Schematic computation flow diagram for calculating clutter cancellation factor.	6
4	Radar antenna groundplane (membrane) coordinate system.	8
5	A representative static deformation mode.	9
6	Schematic drawing of radar antenna groundplane (membrane) showing area (crosshatched) of applied impulse.	9
7	Graphical Fourier space description of deformation modes (center). Two representative deformation modes are at right.	11
8	Graphical Fourier space description of deformation modes (center). Two representative time histories of the amplitudes of the deformation modes are shown at right.	12
9	A collage showing the evolution over time of the Fourier description of deformation of the radar groundplane. The bottom shows the corresponding evolution over time of the deformed groundplane. The graph at top shows the corresponding time series of amplitudes of a single mode.	13
10	Model of Canadian Radarsat radar and an example of a thermal, or quasi-static, deformation (based on a figure in reference 10).	14
11	Example of predicted vibration modes for a model of Canadian Radarsat radar (based on a figure in reference 10).	15
12	Effects of static deformation on DPCA clutter cancellation when no compensation is attempted and when compensation with perfect measurements is attempted.	16
13	Effects of dynamic deformation on DPCA clutter cancellation when no compensation is attempted and when compensation with perfect measurements is attempted.	17
14	Typical groundplane-measurement-system layout.	19
15	An example of a distance-measurement apparatus (as proposed by reference 14) that could be used for multilateration.	19
16	Diagram showing multilateration geometry, including three sensors—A, B, and O—and the point P on the groundplane whose position is to be determined.	20

LIST OF ILLUSTRATIONS (Continued)

Figure No.		Page
17	Interpolation geometry showing the point m whose position is to be determined from its nominal location and the nominal locations of points 1 to 4 that surround it.	20
18	Effects of CCF of an undeformed groundplane of measurement errors having different standard deviations. Results for various sizes of rectangular grids (such as the 4×4 grid in the inset) are shown.	23
19	Effectiveness of compensation for a deformed (as in Figure 5) groundplane of measurements having different standard deviations. Results are for two grid sizes.	23
20	Contour plot of standard deviation of random estimation error normalized to measurement error (equivalent to GDOP of GPS) showing the increase in error at the edge of the antenna.	25
21	Contour plot of estimation-error bias normalized to measurement error showing the nature of the error with increasing measurement accuracy.	26
22	Contour plot showing a comparison of normalized position estimation-error bias (bottom) with the original deformation.	28
23	CCF deficit (defined in text) vs. measurement accuracy for various numbers of measurements and estimated modes.	31
24	Fourier space plot of maximum deformation amplitudes showing the particular modes that were estimated in each case in Figure 23.	31
25	Evolution of deformation showing location of measurement, for a serial measurement scheme, at indicated times; 121 points are measured with a dwell time of 10 msec per point.	32
26	Timelines for prediction of location of each reflector, or measurement grid point, showing sequence of measure, compute, predict for three sequential measurements.	35
27	Timelines for synthesis of location of each reflector, or measurement grid point, showing sequence of (three) sequential measurements, estimation and prediction of mode amplitude, and synthesis of deformation.	36
28	Canonical computation flow diagram for prediction and synthesis of deformation modes.	37
29	Plots of actual (solid curve), measured (dot-dash curve), and predicted (+ 's) mode amplitudes.	39
30	Plots of actual (solid curve), measured (dot-dash curve), and predicted (+ 's) mode amplitudes.	40

LIST OF ILLUSTRATIONS (Continued)

Figure No.		Page
31	Plot of number of modes having less than a given (on x axis) ratio (in dB) of mode amplitude divided by prediction error. High ratios (low relative-prediction errors) are desirable.	42
B-1	Radar antenna groundplane (membrane) coordinate system.	49
B-2	Schematic drawing of radar antenna groundplane (membrane) showing area (crosshatched) of applied impulse.	51
C-1	Diagram showing multilateration geometry, including three sensors—A, B, and O—and the point P on the groundplane whose position is to be determined.	53
C-2	Typical groundplane-measurement-system layout.	55

LIST OF TABLES

Table No.		Page
1	Residual Bias vs. Measurement Error	27
2	Changes That Reduce Frame Time (Skew)	33
C-1	Unknown and Known Parameters of Points	53
C-2	Measurements Used for Multilateration	54

1. INTRODUCTION

Large planar phased arrays are being considered for space-based radar (SBR) applications. If the radar's groundplane is deformed (i.e., not planar), its main beam broadens and may undergo pointing error and sidelobe degradation. If a displaced-phase-center antenna (DPCA) is designed, then clutter cancellation is also degraded.

Usually, these effects are controlled by designing a support structure for the groundplane that is rigid enough to allow the radar to meet or exceed specified performance criteria for quantities such as beam-pointing error, beamwidth, and sidelobe levels. To meet tight tolerances, this approach can lead to massive, elaborate, and expensive support structures for the groundplane.

If a rigid-enough approach is used for an SBR, the effort and expense of constructing a rigid groundplane and the cost per pound of launching it into orbit could become prohibitive. This is especially true considering the desire for the SBR to have a large power aperture product (by having a large aperture which would require an extensive support structure).

Figure 1 shows an example of a conceptual SBR [1] with a 700 m^2 1.4 MW power-aperture product that is achieved mainly by the (nominally $13.8 \times 50.8 \text{ m}$) aperture. The aperture comprises 960 panels (subarrays), each of which is $6 \times 8 \text{ m}$ and radiates 2 kW of average power. In this case, an "RMS uncompensated out-of-plane deflection of the panel phase centers of 4 mm [1]" was thought to be adequate. One conclusion is that it is necessary "to see how. . . [the antenna] could be supported on a light-weight deployable structure . . . [1]."

If the SBR is designed to be rigid enough to satisfy the 4-mm tolerance despite the continual cyclical heating of the antenna as it orbits the earth, then the structure would have little chance of being lightweight and its launch costs would be very high. Costs would be further increased by the need to construct and launch the antenna in separate sections and assemble it in orbit or the need to fold the antenna and deploy it in orbit, where a costly, extensive in-orbit mechanical alignment of the structure would be required. Clearly, the expense associated with launching and aligning a large rigid antenna might be prohibitive.

In contrast, if the antenna groundplane is relatively flexible, or deformable, and if the radiating elements are rephased to compensate for the deformations so that an elaborate in-orbit alignment is unnecessary, then construction of an SBR with a large power-aperture product might be feasible.

1.1 TRADE-OFFS

The rigid-enough approach imposes a trade-off of clutter cancellation performance vs. weight. Any deformation-compensation method will impose a trade-off of clutter cancellation performance vs. the SBR design complexity associated with the compensation method.

Both of these trade-offs ultimately translate to SBR cost vs. performance. However, when cost is considered, the compensation methods will be the clear choice over the rigid-enough approach, because the cost of achieving a given level of performance using compensation is likely to be dramatically less than the cost of achieving performance by increased rigidity (and weight).

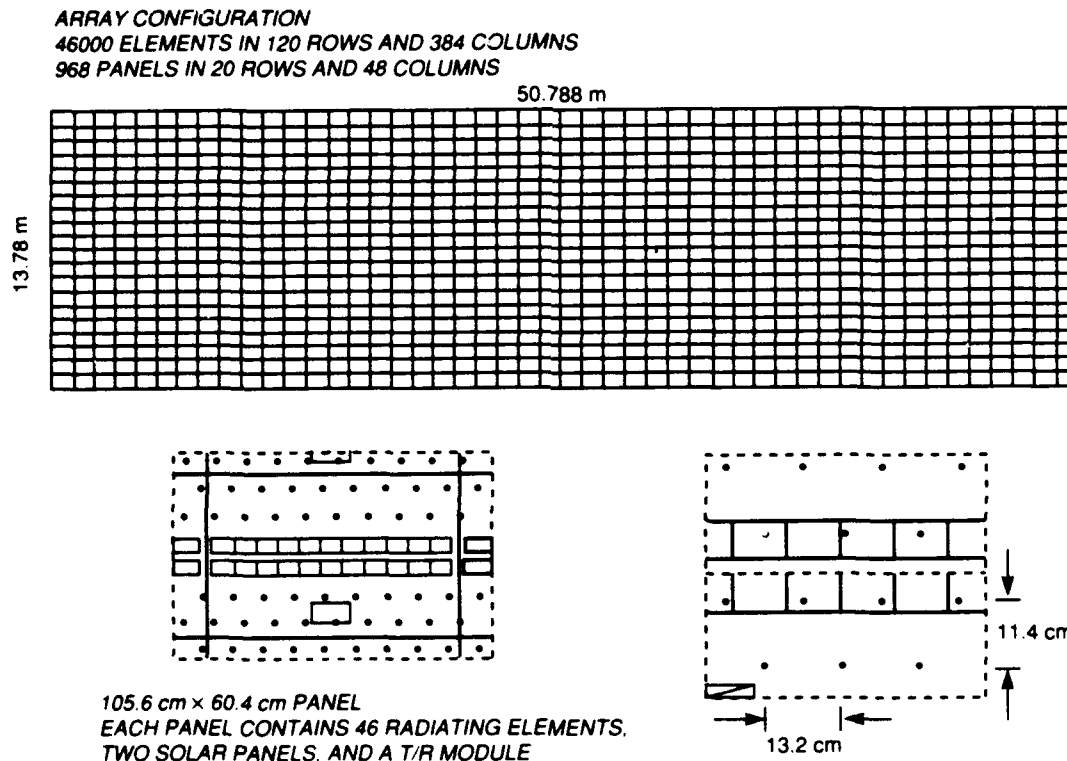


Figure 1. Conceptual design for a large space-based radar.

1.2 PREVIOUSLY PROPOSED METHODS OF COMPENSATING FOR DEFORMATIONS

Two different methods of compensating a radar for deformations have been described. One method examines properties of the electromagnetic waves that comprise the radar pulse returned by clutter and picks an appropriate signal-processing algorithm depending on these properties. A summary of these methods can be found in a report written by Attia [2]. The processing algorithms depend on finding [3] or synthesizing [4] a dominant scatterer in the radar beam or determining the location of all the radiating elements of a phased array by cross correlating the returned radar pulse received by two antenna elements and using the correlation lag to rephase the antenna's radiating elements [5].

A second method involves use of beacons that broadcast an electromagnetic signal whose phase at various receivers is used to determine their location [6].

The deformation-compensation method that will be described here is similar to the second method, except that laser light is used in place of radar-wavelength electromagnetic waves.

1.3 OUTLINE OF REPORT

The first section of this report describes the objectives for performing this work. The next sections describe the model SBR, the radar beam-pointing algorithm, the measure of performance of DPCA, which is the clutter cancellation factor (CCF), and the deformation model assumed in the analysis. To demonstrate the validity of the deformation model used here, there is a comparison to a prediction of deformations of the Canadian Radarsat synthetic aperture radar (SAR). The effects of uncompensated deformations on the CCF are then presented.

Next, the proposed method of estimating deformations—multilateration—and its ameliorating effects on clutter cancellation are described. A problem of implementing multilateration is then described, a solution for the problem is presented, and some results of a simple analysis of the solution's feasibility are described.

2. OBJECTIVES

The objectives of this work were to explore deformation compensation for a flexible antenna groundplane and to establish the feasibility of the complexity-vs.-performance trade-off presented previously. In doing this, answers to these questions were sought:

- What elements would a typical compensation system comprise?
- What measurements would the compensation system make?
- How accurate must the measurements be?
- How much will compensation for deformations improve clutter cancellation performance?
- Does a dynamic structure pose any particular problem for compensation?
- Can the knowledge of the dynamics of the structure improve estimates of deformation?

2.1 SBR ANTENNA MODEL

The radar antenna model used to investigate deformation compensation (Figure 2) was suggested for testing SBR concepts. The groundplane's nominal dimensions are 8.2×2.2 m, and it is populated with monopoles on a hexagonal grid. The grid spacing is 0.156×0.136 m along the 8.2 m and 2.2 m directions, respectively. The radar frequency is 1.3 GHz (0.23 m wavelength — L band). Two non-overlapping receive phase centers are used for DPCA.

2.2 ALGORITHM FOR STEERING THE ANTENNA

For the usual nominally planar antenna, steering is accomplished by phasing each radiating element according to its nominal location and the desired steered point, so that an element with coordinates x_m, y_m will be set to have phase ϕ_m if the radar is steered to angles θ_0, ϕ_0 :

$$\phi_m = -2\pi \{x_m \cos(\phi_0) + y_m \sin(\phi_0)\} \sin(\theta_0) / \lambda \quad (1)$$

The algorithm used here for a deformed antenna is the extension of the above to account for a z coordinate that is no longer 0 because a deformation is present. The phase of the m th radiating element will become $\phi_{m,DEF}$ if its estimated z coordinate is z_m :

$$\phi_{m,DEF} = -2\pi \{[x_m \cos(\phi_0) + y_m \sin(\phi_0)] \sin(\theta_0) + z_m \cos(\theta_0)\} / \lambda \quad (2)$$

2.3 CLUTTER CANCELLATION

The measure of performance of deformation compensation used throughout this work is the clutter cancellation factor (CCF), which is a measure of the cross correlation, integrating over all space, of the two receive beams weighted by the transmit beam [7]. CCF is a measure of residual clutter power after DPCA processing relative to raw clutter power.

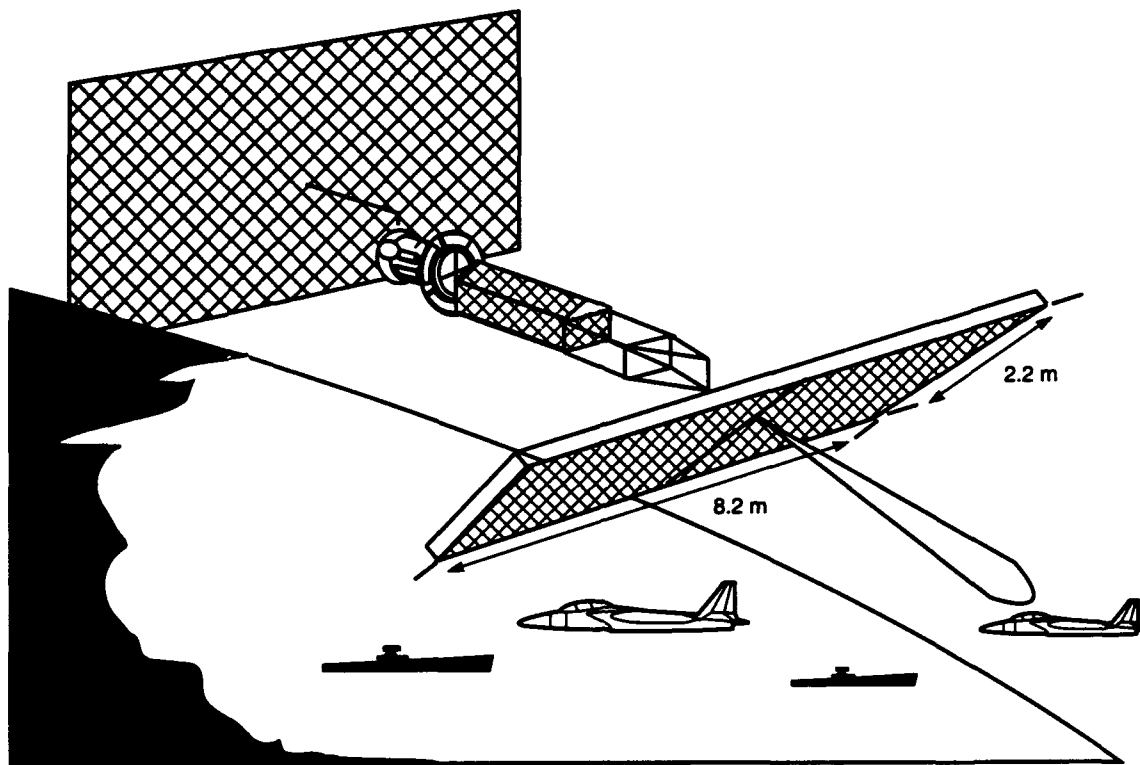


Figure 2. Radar antenna used to investigate effects of deformation.

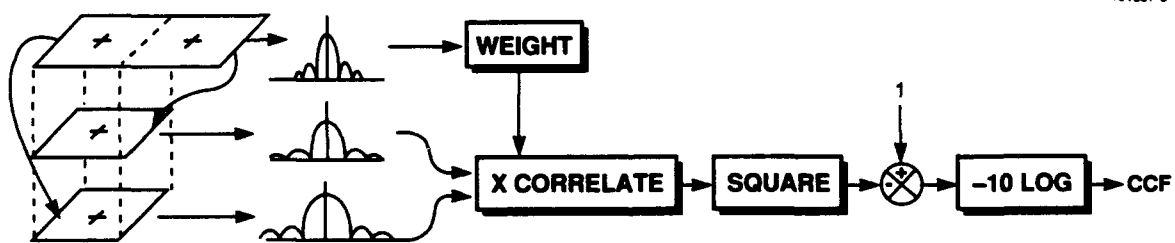


Figure 3. Schematic computation flow diagram for calculating clutter cancellation factor.

The schematic computation diagram flow in Figure 3 depicts the calculation of the CCF. The details of the calculation have been included in Appendix A. At the top left of Figure 3 is the transmit aperture of the radar. The two receive apertures, separated by a dotted line, are shown superimposed on the transmit aperture. The next line down shows the leading receive aperture; the trailing receive aperture is shown on the bottom line. The various apertures are shown on different lines because they are in effect different inputs to the CCF computation.

The electric-field patterns of the two receive apertures are calculated (as shown in the next step to the right in the process) and cross correlated over all space using the squared magnitude of the transmit electric field pattern as a weight; this is also shown above the two receive patterns. The phase of each of the electric field patterns for each aperture is computed relative to the average phase center, which is assumed to be at the geometric center of the aperture [7]. The magnitude of the cross correlation is then squared, subtracted from one, and expressed in decibels.

The two receive apertures of an undeformed groundplane will have a cross correlation equal to 1 and consequently will produce an infinite CCF. Clutter will be completely cancelled in this case. In contrast, deformations that completely decorrelate the two receive apertures will have no cross correlation (i.e., the result is zero), so the CCF will be 0 and residual clutter will be high.

2.4 GROUNDPLANE DEFORMATION MODEL

Deformations can be classified into two groups: static, or very slowly varying over time (quasi-static), and dynamic. The distinction is somewhat blurred, but static deformations will be assumed to include quasi-static ones. Here, quasi-static means changing with a period that is greater than tens of minutes, or about one tenth of the orbit period. Static and quasi-static deformations are caused by stress relief and thermal deformations that occur as the orientation of the SBR relative to the sun changes during the orbit.

Dynamic deformations, or vibrations, may also occur. These are caused by equipment that vibrates and, more likely, by station keeping of the SBR, which will need to be continually yawed if DPCA is used [8]. Any thruster impulse during station keeping may excite vibrations.

Investigating the effectiveness of compensating for deformations requires a model of the SBR's structure. As a detailed SBR design is unavailable, a simple model that includes relevant features of the deformation of structures will suffice. For this work, the antenna's groundplane was modeled as a stretched rectangular membrane. The details of this approach are presented in an appendix.

The physics and associated mathematics of vibrations of the model groundplane lead to descriptions that involve normal modes. In essence, these are vibrations with definite spatial patterns and definite frequencies. If the groundplane is excited with a force that oscillates at the mode frequency, then the groundplane will naturally attempt to vibrate with the definite spatial pattern of the mode.

For the selected model, the deformation $z_{m,n}(x,y,t)$ produced by a mode is the product of two cosines and a function of time;

$$z_{m,n}(x,y,t) = T_{m,n}(t) \cos(\pi x / L_x) \cos(\pi y / L_y) \quad , \quad (3)$$

where m and n are positive integers that may be used to uniquely designate the mode and where $0 \leq x \leq L_x$ and $0 \leq y \leq L_y$. (The origin of coordinates is at the lower left corner of the antenna as viewed from a point on the positive portion of the z axis — see Figure 4.) The product and the arguments of the cosines are determined by the boundary conditions imposed on the groundplane.

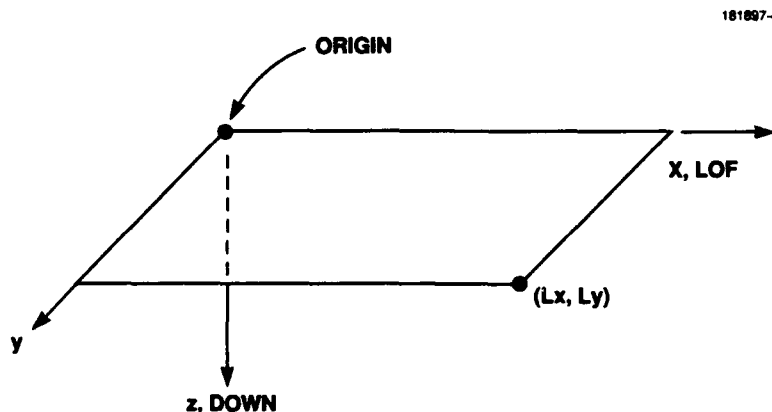


Figure 4. Radar antenna groundplane (membrane) coordinate system.

Both static and dynamic deformations were used to illustrate properties of a deformation compensation system. For a static case, $T_{m,n}$ was assumed to be a constant:

$$T(t)_{m,n} = A_{m,n} \quad (4)$$

Also, $m = 2$ and $n = 2$ were assumed so that the deformation was

$$z(x,y)_{\text{STATIC}} = A_{2,2} \cos(2\pi x / L_x) \cos(2\pi y / L_y) \quad (5)$$

This deformation (Figure 5), with $A_{2,2} = 25$ mm, for example, would presumably be produced by a force on the antenna's groundplane due to a thermal gradient.

The dynamic case that was considered was the response of the groundplane to an impulse. The impulse was assumed to be upward directed and uniformly distributed (Figure 6) over the central quarter of the groundplane for which $L_x/4 \leq x \leq 3L_x/4$ and $L_y/4 \leq y \leq 3L_y/4$. This might be produced by a misalignment of an azimuth thruster. The distribution of the impulse was assumed to be uniform because the central part of the groundplane is near the instrument package and may be stiffened as a result.

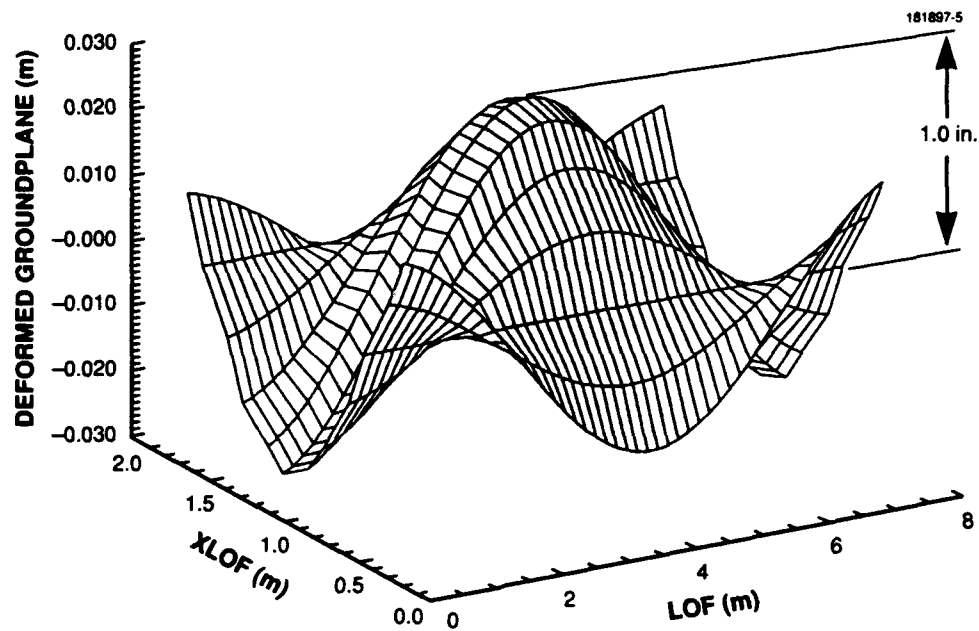


Figure 5. A representative static deformation mode.

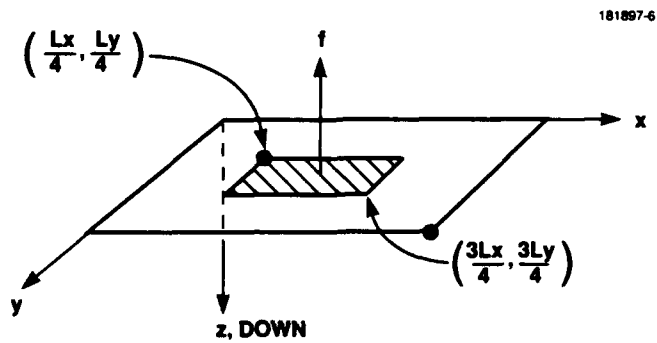


Figure 6. Schematic drawing of radar antenna groundplane (membrane) showing area (crosshatched) of applied impulse.

Derivations in Appendix B show that for the assumed impulse, the amplitude $T_{m,n}$ is a decaying sinusoid whose frequency is the mode frequency and whose maximum amplitude is determined by the spatial distribution of the impulse for the exciting force that is considered here. The deformation of the groundplane is then given by an infinite Fourier series of terms:

$$z(x,y,t) = \sum_{n>0, m>0} T_{m,n}(t) \cos(\pi n x / L_x) \cos(\pi m y / L_y) \quad (6)$$

A method of visually representing mode amplitudes in this Fourier series is to devise a coordinate system whose x' and y' coordinates are the arguments of the cosines that comprise the product and whose z' coordinate is the absolute value of the amplitude, viz.:

$$x' = 2\pi n / L_x \quad (7)$$

$$y' = 2\pi m / L_y \quad (8)$$

$$z' = |T_{m,n}(t)| \quad (9)$$

The points (x', y', z') may then be plotted.

All of the modes of a vibration are now represented as a set of points in (x', y', z') space whose z coordinates oscillate between 0 and a maximum value determined by the exciting force. To give these points visual integrity for display purposes, they are connected by line segments to form a segmented surface as shown in the left portion of Figure 7. The shape of the surface changes with time.

The right-hand portion of Figure 7 also shows the maximum amplitude of two modes that are associated with two points of the amplitude surface. Note that the mode in the upper right is the same as the static deformation shown earlier. However, in the case of vibrations, this mode is only one of many; its amplitude will oscillate with time and will periodically be zero, as shown in Figure 8.

Figure 8 shows plots of $T_{m,n}(t)$ for the modes shown in Figure 7. Note that the periods and amplitudes of the two modes are different.

The vibrations excited by the assumed impulse are shown in Figure 9, the bottom of which shows a series of "snapshots" of the deformation from the instant the impulse occurs until after the spreading deformation wave reflects off the edge of the groundplane (a mass discontinuity) and begins to converge again toward the center of the groundplane. The evolution over the same time interval of the amplitude surface and of the amplitude of one mode is also shown.

The damping and restoring constants, mass density, etc., to produce the deformations shown in Figure 9 were chosen to produce reasonable wave speed and damping. The restoring force constant was sized by requiring that the $n = 1, m = 0$ mode have a period of 5 seconds. This resulted in a deformation wave speed of 1.6 m/s regardless of direction of propagation. The time constant for damping was chosen to be 30 seconds regardless of mode; consequently, the model is slightly dispersive.

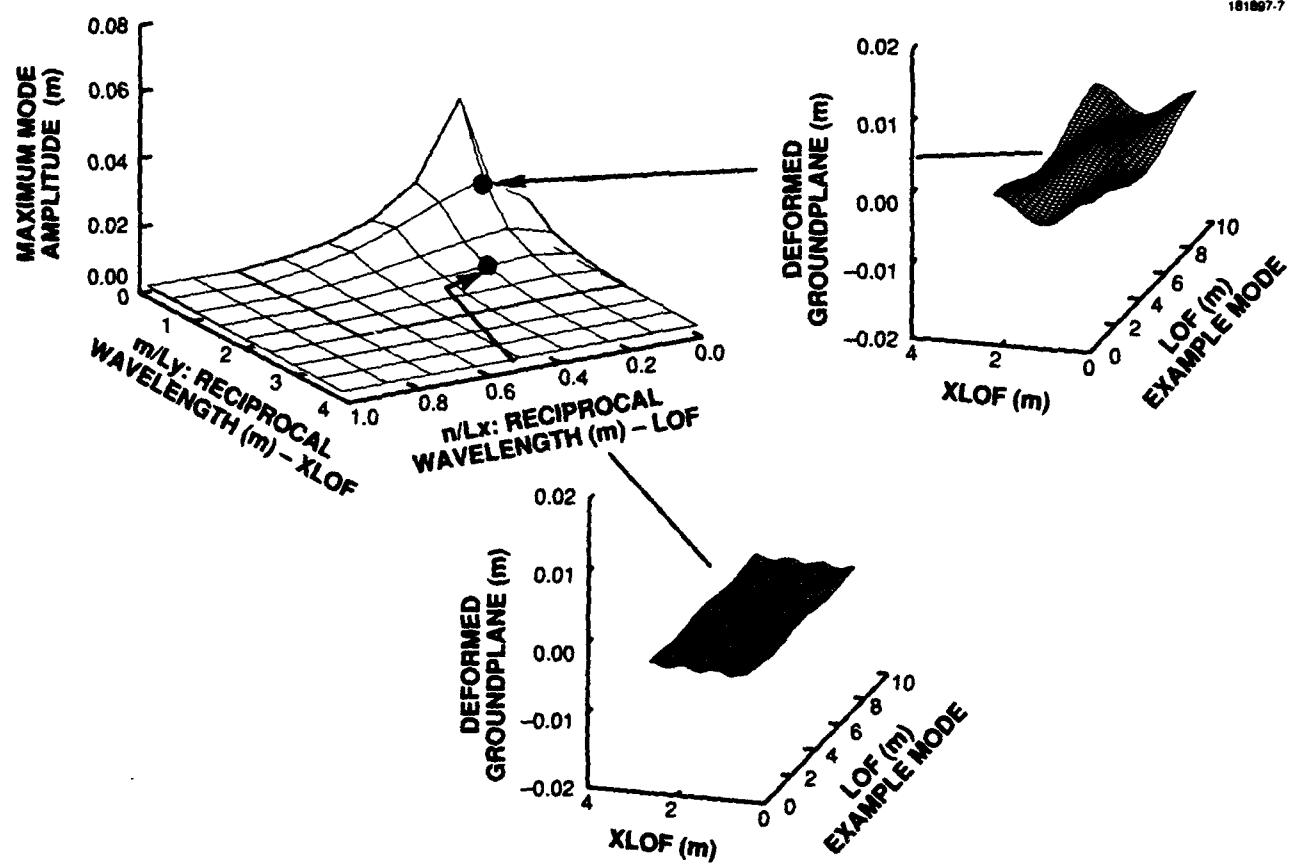


Figure 7. Graphical Fourier space description of deformation modes (center). Two representative deformation modes are shown at right.

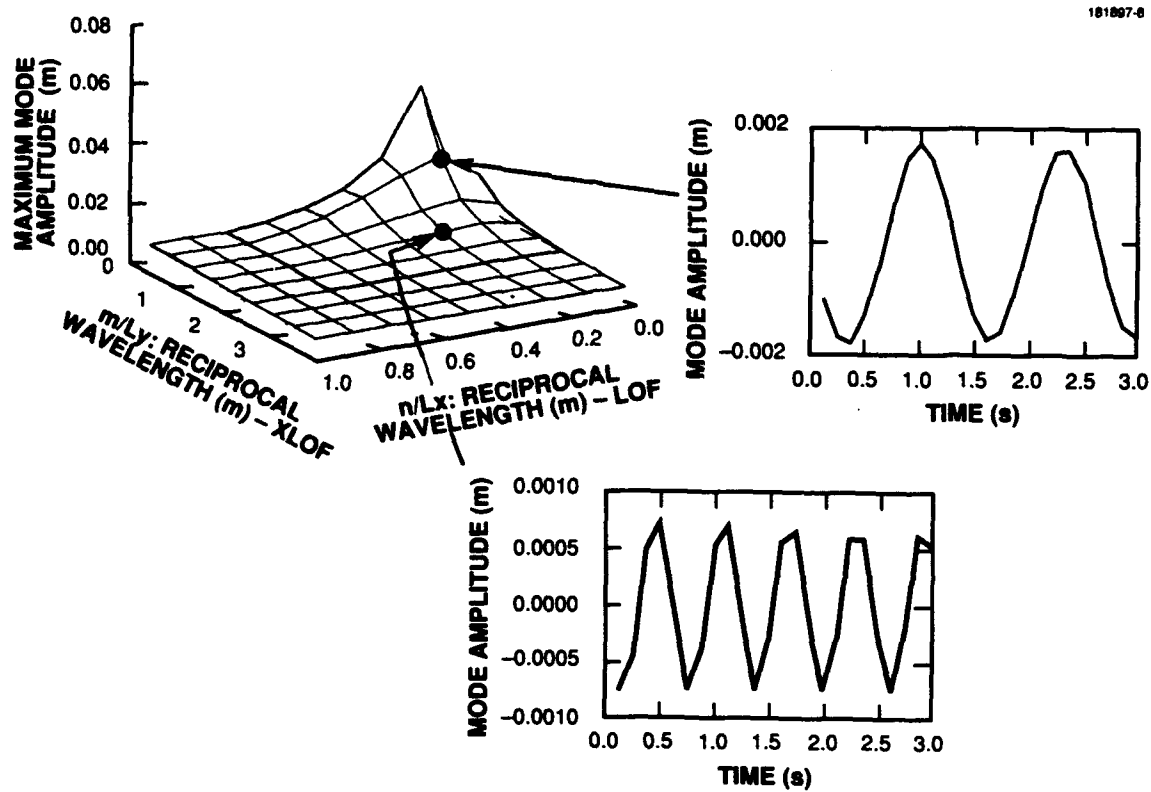


Figure 8. Graphical Fourier space description of deformation modes (center). Two representative time histories of the amplitudes of the deformation modes are shown at right.

The deformations shown in Figure 9 were produced by truncating the Fourier series at $m = 8$ and $n = 8$ modes so that 81 modes were used to produce the deformations in the figure. The frequencies of the modes range from 0.2 Hz (the fitting frequency described above) to 6.23 Hz. Of the 81 possible modes used, 15 ($m = 6$, all n , and $n = 6$, all m) are zero; approximately 20 are significantly different from zero.

181807-9

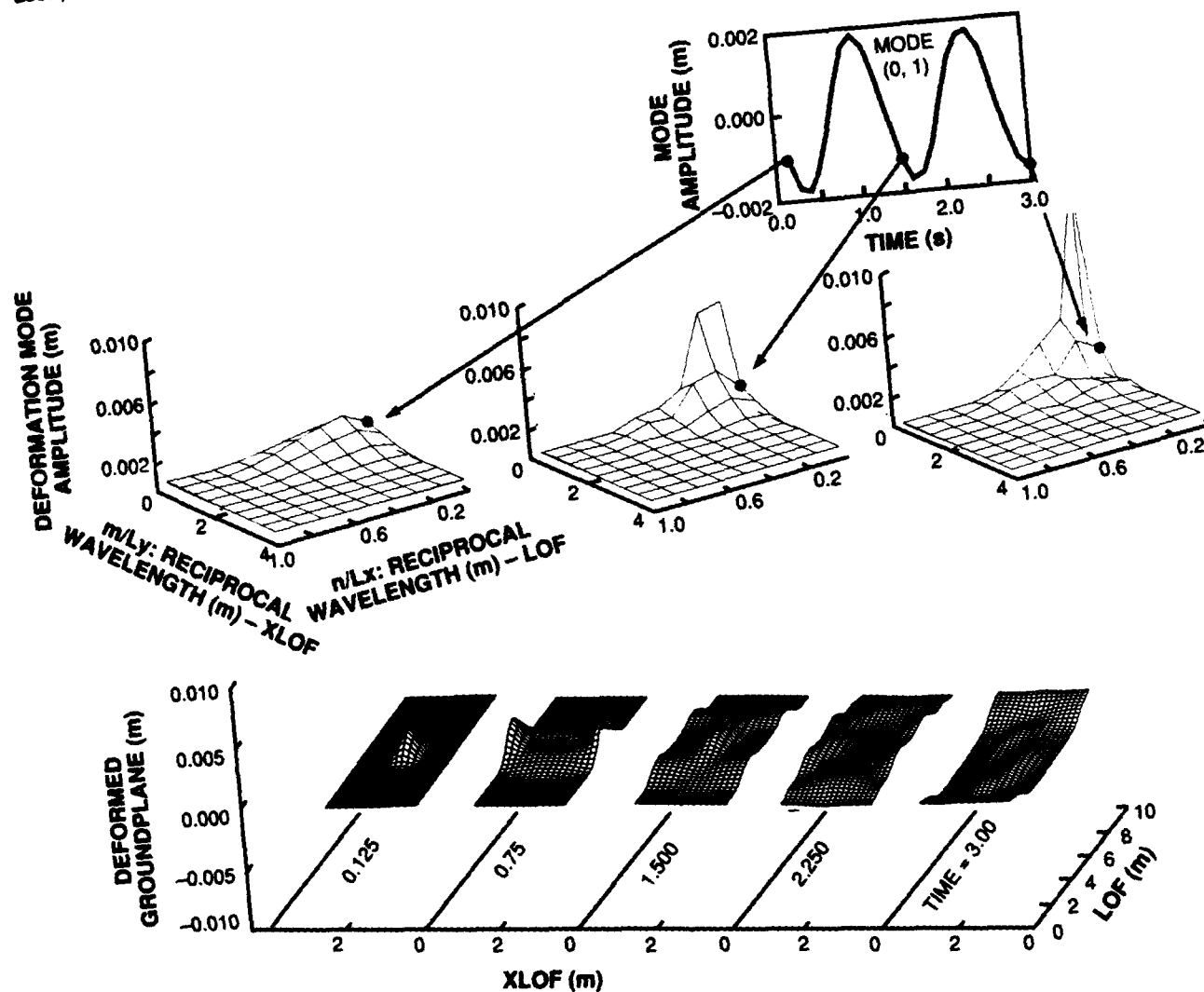
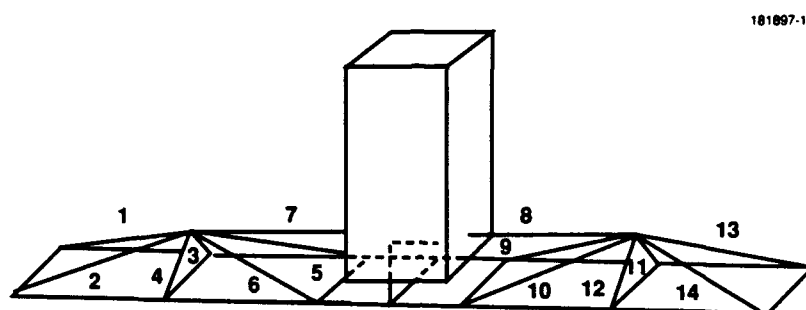


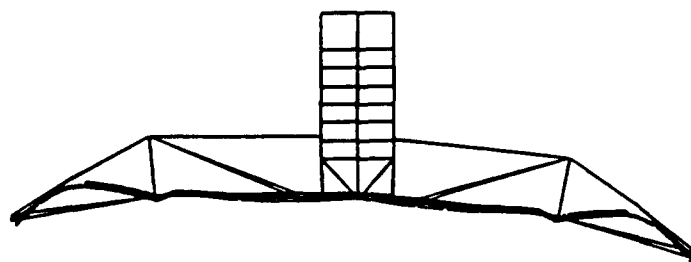
Figure 9. A collage showing the evolution over time of the Fourier description of deformation of the radar groundplane. The bottom shows the corresponding evolution over time of the deformed groundplane. The graph at top shows the corresponding time series of amplitudes of a single mode.

The significance of being able to approximately describe deformations by a few (9–20) modes out of an infinite set transcends the convenience of the model for computations involved in this study. The necessity to predict the structure's future deformations by some method will become apparent. The possibility of obtaining accurate approximate descriptions of deformations by using 9–20 modes bodes well for any attempt to use a model of the structure in a Kalman filter to predict the structure's future behavior from a set of measurements and accumulated estimates.

The features of the simple model described are also present in a much more elaborate (582 element, 400 node) finite-element model (FEM) that was used to predict the deformations of the Canadian Radarsat SAR [9]. Figure 10 shows a static deformation predicted by the model and Figure 11 shows two predicted vibration modes, one symmetric, the other antisymmetric.

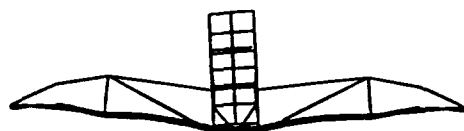


UNDEFORMED STRUCTURE (Note Symmetry)



THERMAL (Quasi-Static) DEFORMATIONS
– 12.43 mm TIP DISPLACEMENT

Figure 10. Model of Canadian Radarsat radar and an example of a thermal, or quasi-static, deformation (based on a figure in reference 10).

**FIRST VIBRATION MODE**

- SYMMETRIC GROUNDPLANE DEFORMATION
- 3.5 Hz

**SECOND VIBRATION MODE**

- ANTI-SYMMETRIC GROUNDPLANE DEFORMATION
- 5.0 Hz
- NOTE HILLS AND VALLEYS IN GROUNDPLANE

Figure 11. Examples of predicted vibration modes for a model of Canadian Radarsat radar (based on a figure in reference 10).

In comparison to the 8.2×2.2 m radar antenna model used here, the undeformed Radarsat SAR groundplane size is 12×1.5 m. Both models exhibit vibration-mode frequencies up to 6 Hz. In addition, the Radarsat SAR FEM predicts deformations up to about 0.5 inch. Deformations of up to 1 inch are considered for the simple model used here.

Both SBR models are symmetric; as a consequence their vibrations will be either symmetric or antisymmetric¹, but not both. Symmetry refers to the result of interchanging two opposing sides of a structure by reflection through a vertical plane that is parallel to one of the sides and bisects the structure. For a symmetric structure, this leaves the structure unchanged.

The comparison shows that the model used here has a number of relevant features in common with a more elaborate model that should accurately describe a buildable SBR. In part, this occurred by judiciously choosing the few physical constants of the simple model, but it was also due in part to fundamental properties of the model, such as symmetry.

2.5 EFFECTS OF UNCOMPENSATED DEFORMATIONS OF CLUTTER CANCELLATION

If the groundplane deforms and DPCA is used to cancel clutter, cancellation will be degraded and performance will suffer unless mitigating procedures are used.

¹ For the simple model, modes with odd m or odd n are antisymmetric.

The effects of simple deformations for Gaussian radar beams has been studied previously [10], but the effects of the deformations used here have never been determined for actual beam patterns to be used by an SBR.

Figure 12 shows the effect of the canonical static deformation on clutter cancellation. The amplitude of the deformation (the maximum displacement achieved by any point in the groundplane) is indicated on the x axis. The shape of the deformation for the calculations summarized by the curves (inset) was held constant. The usual SBR design goal of 50 dB of clutter cancellation is indicated by the dotted line.

The lower, "no compensation," curve shows the clutter cancellation for an SBR without groundplane compensation. As deformation amplitude increases, the CCF steadily degrades, and it is below 50 dB for all deformations exceeding 0.64 mm. In this case, the antenna elements are phased according to their nominal locations on the groundplane, as if the deformations were not present.

The upper, "no measurement error," curve shows clutter cancellation for an SBR that employs groundplane compensation and for a groundplane measurement system that has no measurement errors. Here, the antenna elements are phased according to the (perfect) estimates of their actual location. This

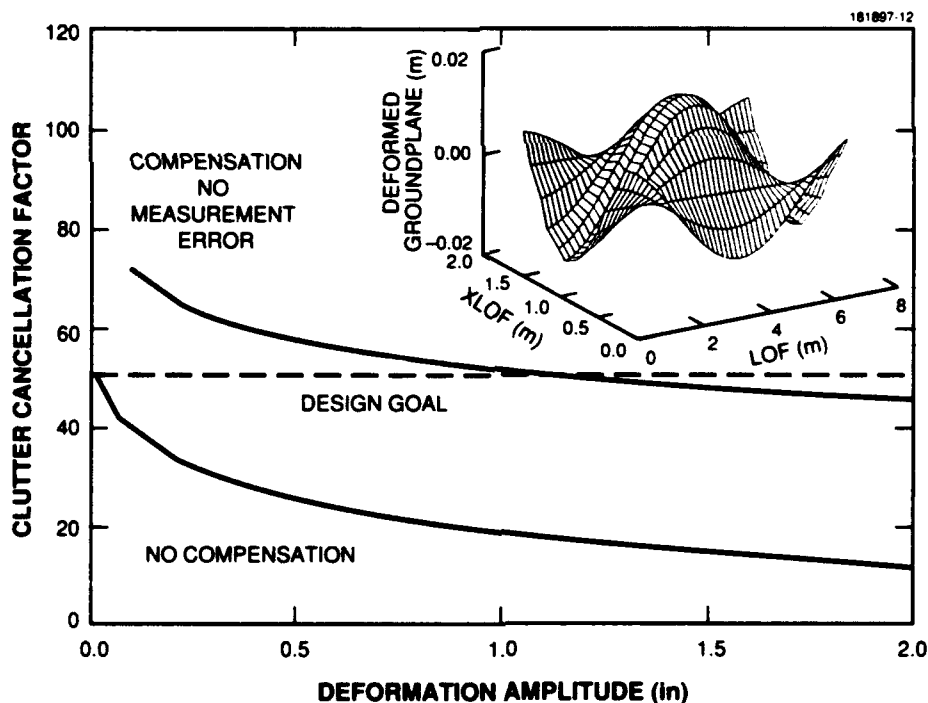


Figure 12. Effects of static deformation on DPCA clutter cancellation when no compensation is attempted and when compensation with perfect measurements is attempted.

is in contrast to the usual situation described previously. If a design goal for a groundplane measurement system were to compensate for the deformations so that the CCF was above 50 dB, then a perfect system would have allowable deformation of about 1 inch.

For an impulse excitation, Figure 13 shows the two curves that correspond to those just described for the static deformation. The collage on the top line is a repeat of one given earlier and is a description of the deformations for which the CCF was calculated.

The CCF-vs.-time for a perfect system (no measurement errors, estimates essentially all modes) is shown as a solid line in the graph. The CCF for a worst case (a radar phased according to the nominal position of its radiating elements) is also shown. The maximum deformation of any point in the groundplane over the 3-second interval shown is slightly less than 1 inch.

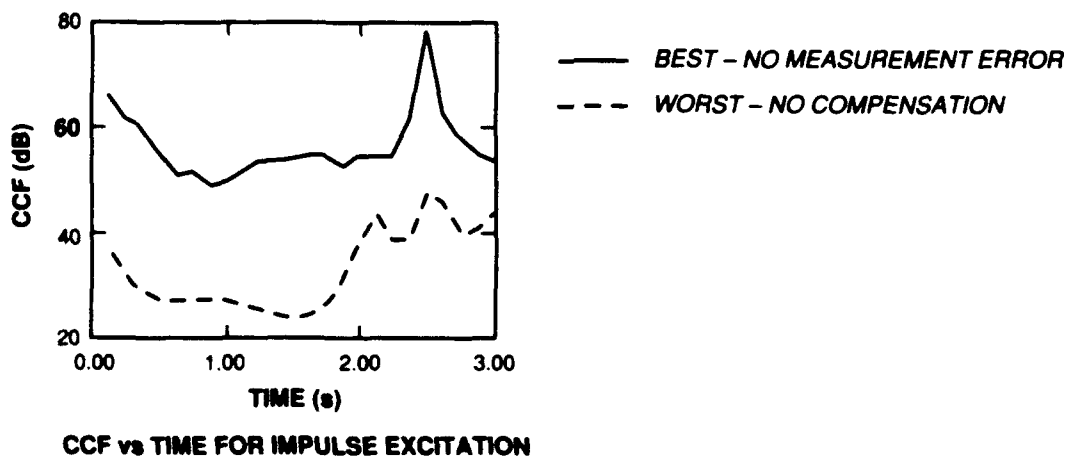
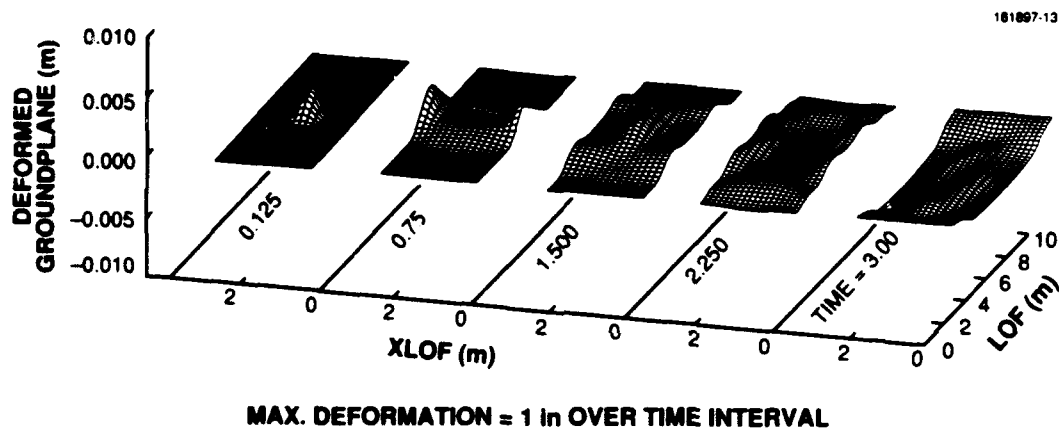


Figure 13. Effects of dynamic deformation on DPCA clutter cancellation when no compensation is attempted and when compensation with perfect measurements is attempted.

Recall that for the static deformation 1 inch is the amplitude at which the 50 dB design goal can be achieved with no reserve performance. Apparently, for a compensated vibrating deformation with about the same amplitude, the 50 dB goal can always be achieved regardless of the shape of the deformation as it evolves in time; sometimes there will even be reserve performance.

Having shown that a perfect system can achieve desired performance and realizing that real compensation systems will have measurement and other errors, the next subject to be explored is a conceptual system that would have typical errors. This conceptual study will pin down the allowable magnitudes of the errors; the effects of the errors will then be described.

2.6 ESTIMATING DEFORMATIONS — MULTILATERATION

Estimating deformations is essentially a surveying problem. The tasks of surveying are to establish a coordinate system for the measurements, then locate objects relative to that system. In the current SBR application, the objects to be located are points on the groundplane. The coordinate system can be constructed for convenience; actually, two convenient systems, one for making measurements and one for phasing the radiating elements, exist.

Two methods of estimating the location of objects were considered, triangulation and multilateration. The first method uses measurements of angles and distances to locate objects; the second uses only measurements of distance. The first is generally familiar²; the second is used by the Global Position Satellite System [11]. Multilateration was selected for analysis.

Multilateration requires a set of active transmitter/sensor elements to form the measurement coordinate system and a set of reflectors or perhaps receivers mounted primarily on the groundplane to determine its deformed shape (see Figure 14).

Either radio-wavelength transmitters and receivers or lasers with beam directors and optical reflectors could be used as the sensors for multilateration. Problems associated with radio wavelengths are multipath (because narrow radio beams are not available) and bias problems associated with path lengths in waveguides, etc. Biases can be estimated as part of the larger problem of locating a point on the groundplane, but this increases the number of required measurements from three to four or more per point.

Lasers inherently have narrow beams, and consequently no multipath; they are currently being used in commercial systems to locate objects and develop contours of surfaces. Currently manufactured versions of these systems have a coherence length (maximum distance that an object can be from the laser) of about 5–10 m, which makes them unsuitable for an SBR application. Recently, however, a laser with about 1.5 km coherence length [12] has been developed at Lincoln Laboratory, so this is no longer a concern. Figure 15 shows a schematic drawing [13] of a commercial laser measurement system.

² For an example, see A.C. Doyle, "The Musgrave Ritual."

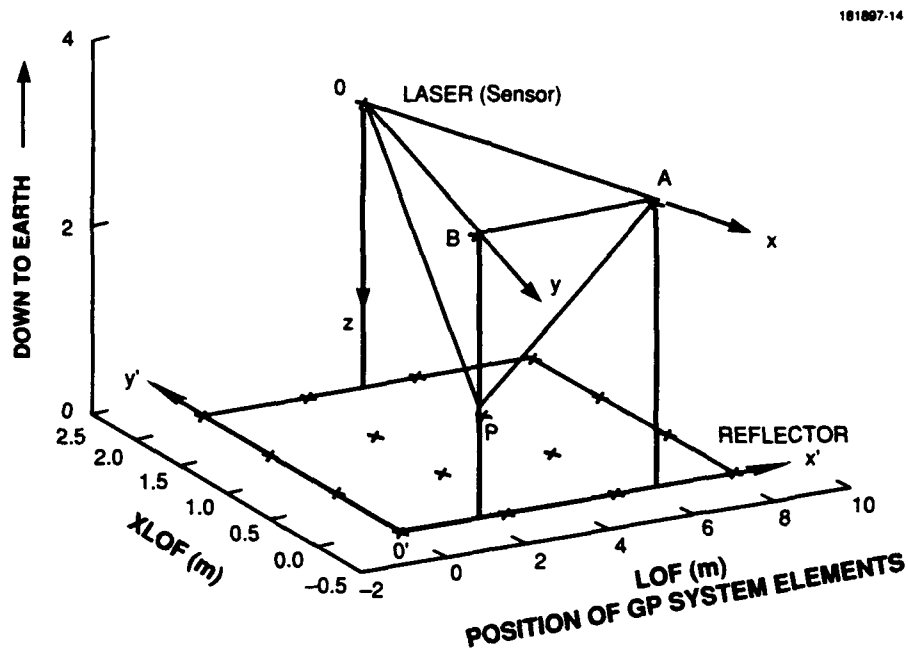


Figure 14. Typical groundplane-measurement-system layout.

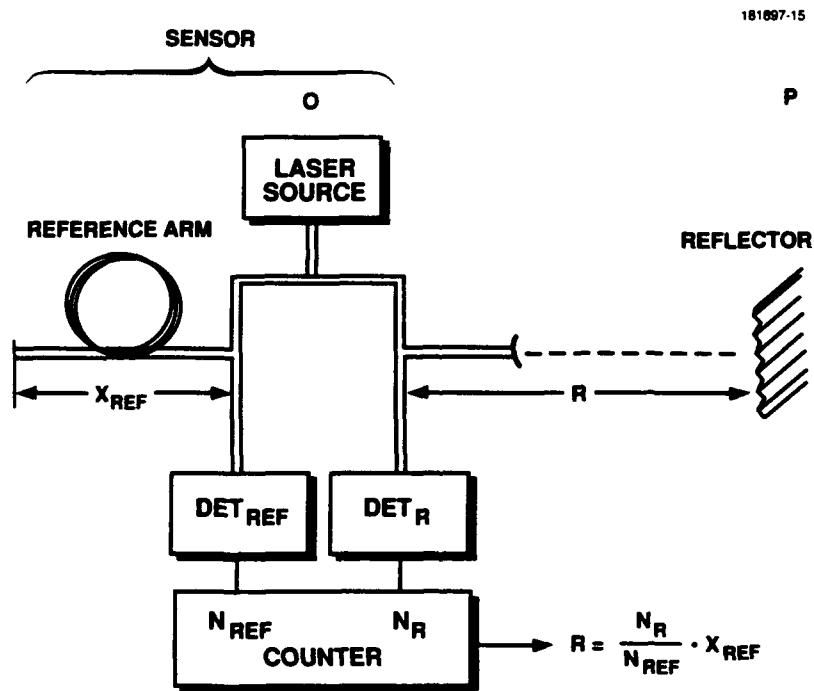


Figure 15. An example of a distance-measurement apparatus (as proposed by reference 14) that could be used for multilateration.

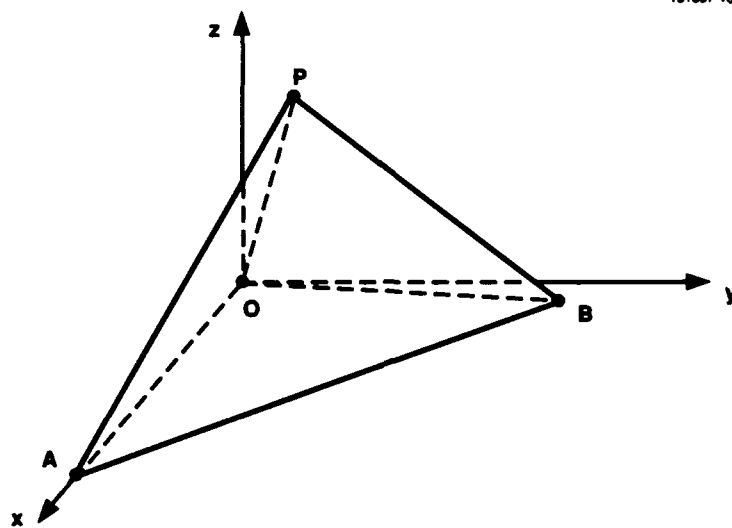


Figure 16. Diagram showing multilateration geometry, including three sensors — A, B, and O — and the point P on the groundplane whose position is to be determined.

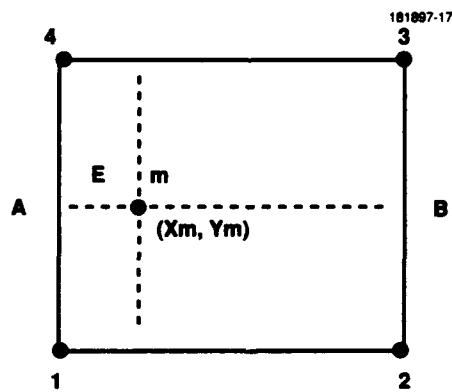


Figure 17. Interpolation geometry showing the point m whose position is to be determined from its nominal location and the nominal locations of points 1 to 4 that surround it.

The system works as follows: the laser beam is phase modulated and split; one half travels down an optical fiber of known length (left of center) and returns while the other half travels to the reflector and back (right of center). Both beams are demodulated to produce beat frequencies, which are counted. The unknown distance R to the reflector is determined relative to the known fiber length X_{REF} by a simple ratio calculation shown in the figure.

The laser/fiber/counter electronics, a beam director, and a reflector(s) would be used as sensors in the canonical measurement system (see Figure 14). The reflectors would also be separate system elements mounted in a rectangular grid on the groundplane.

Figure 16 shows a canonical multilateration geometry and the elements of the system. The measurement coordinate system shown in the figure is constructed as follows: Sensor O is defined to be at the origin, A is defined to be on the x axis at an unknown distance from the origin, O, B is defined to be in the first quadrant of the x,y plane; its coordinates (except $z = 0$, which is known by definition) are unknown, and P is defined to have a positive z coordinate with its other coordinates unknown.

The distances between the four system elements at the points of the pyramid, taking the points in pairs, are measured. There are six unknowns, the coordinates x_A , x_B , y_B , x_P , y_P , and z_P of points A, B, and P, respectively. The coordinates may then be calculated (see Appendix C) from the measurements.

The elements of Figure 16 are also shown in a system context in Figure 14. The canonical geometry has been drawn on top of the system layout. The pyramid OABP shown in the last figure has been turned over here. The laser (sensor) at point O and the reflector at point P are shown. Sensors such as the one at O are at points A and B also. The primed coordinate system mentioned above is the second convenient one for phasing antenna elements.

In the figure, there is a 4×4 grid of xs on the groundplane. Each one represents a reflector for the groundplane measurement system. The position of each reflector is measured by the system and the positions of other points on the groundplane, i.e., the radiating elements, are determined by interpolation or some other method (such as direct calculation from mode amplitudes, which will be discussed later).

For static deformations, two-dimensional linear interpolation was used for all calculations of the estimated position of radiating elements. Figure 17 shows a typical interpolation situation. The radiating element E is surrounded by a rectangle formed by four grid points whose coordinates are x_i, y_i, z_i and which are designated by subscripts $i = 1, 2, 3, 4$. The grid points are numbered counterclockwise around the rectangle, beginning in the lower left corner.

For the linear interpolation used here, the z coordinate (deformation), z_m , of the m th radiating element, whose nominal coordinates are x_m, y_m , was estimated by

$$\hat{z}_m = \hat{z}_A + \frac{(\hat{z}_B - \hat{z}_A)}{\Delta x_{14}} \Delta x_{1m} \quad ,$$

because

$$\hat{z}_A = \hat{z}_1 + \frac{\Delta \hat{z}_{14}}{\Delta y_{14}} \Delta y_{1m}$$

$$\hat{z}_B = \hat{z}_2 + \frac{\Delta \hat{z}_{23}}{\Delta y_{14}} \Delta y_{1m}$$

and

$$\Delta y_{im} = \Delta y_{2m} \quad \text{and} \quad \Delta y_{14} = \Delta y_{24} \quad , \quad (10)$$

where

$$\Delta x_{ij} = x_j - x_i \quad (11)$$

and Δy_{ij} and $\Delta \hat{z}_{ij}$ are defined similarly.

2.7 RESULTS: STATIC DEFORMATION

The deformation measurement system will suffer measurement errors and interpolation errors. Measurement errors are assumed to be Gaussian distributed with zero mean and a given variance that depends on the measurement accuracy.

One way to become familiar with the effects of measurement errors in isolation from interpolation errors is to look at the clutter cancellation that can be obtained by measuring the deformations of an undeformed, or planar, groundplane. Figure 18 shows a plot of the effects of measurement error on CCF for an undeformed groundplane (inset).

To a good approximation, the CCF is inversely proportional to the square of the standard deviation of the measurement error or its variance (recall that the measurement errors have been assumed to be unbiased).

An undeformed groundplane was used in an attempt to isolate the effects of measurement error from the effects of interpolation when deformations are present. Interpolation was used, but any errors that resulted were caused by interpolation between points with estimated positions in error (i.e., measurement errors only), not by linear interpolation of a curved surface.

Each line in the figure indicates the size of the interpolation (reflector) grid used. As might be expected, interpolation grid size is not critical for a bland, undeformed surface.

Figure 19 shows the clutter cancellation that can be obtained by compensating a deformed surface using estimated deformations. Note that for measurement error standard deviations that are larger than 1 inch, the CCF for an SBR with a compensated, deformed groundplane (the present case) is qualitatively similar to an SBR with a compensated, undeformed groundplane (which was shown in the previous figure).

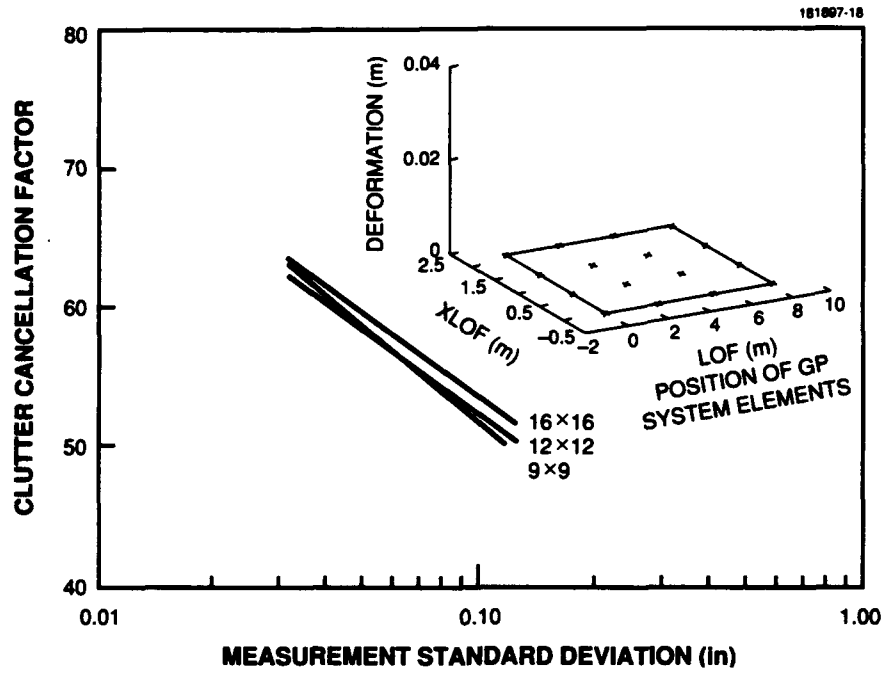


Figure 18. Effects on CCF of an undeformed groundplane of measurement errors having different standard deviations. Results for various sizes of rectangular grids (such as the 4×4 grid in the inset) are shown.

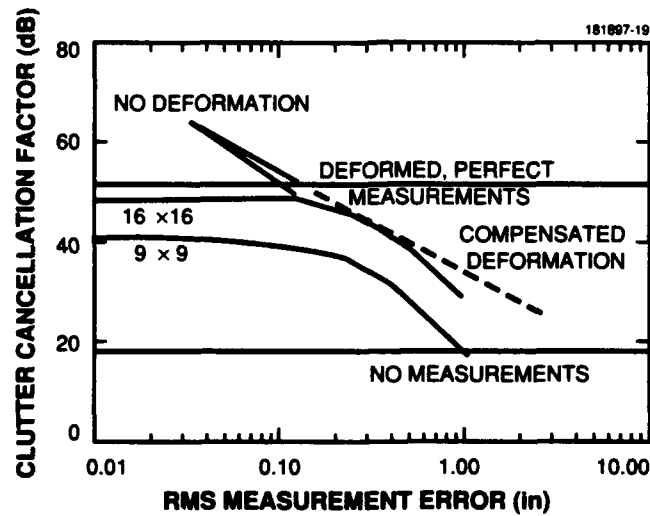


Figure 19. Effectiveness of compensation for a deformed (as in Figure 5) groundplane of measurements having different standard deviations. Results are shown for two grid sizes.

This may be seen by comparing the curves for the two grid sizes, which are for a deformed groundplane, with the lines in the "NO DEFORMATION" region of the figure. These lines have been transferred from the previous figure, and in one case extended, to allow comparison of the rate of decrease of CCF for the two cases. The extended lines representing the CCF for groundplanes with "NO DEFORMATION" are never exceeded, and the CCF for "COMPENSATED DEFORMATIONS" decrease more rapidly than the former.

When the groundplane is deformed, the interpolation grid size becomes important. This may be seen in Figure 19 by comparing the two curves, which intersect the left vertical axis at 41 and 48 dB, respectively. The interpolation grid sizes are shown near the intersection. Note that although the 16×16 grid contains three times as many interpolation grid points (sensors) as the 9×9 grid does, there is a factor-of-five improvement in the CCF (7 dB increase in CCF for 5 dB increase in sensors).

Figure 19 shows that when the random measurement error is sufficiently small, the CCFs for the two interpolation grids become constant and the curves become horizontal because random errors that occur when distances are measured become smaller than interpolation errors, which are roughly independent of measurement errors and depend on grid size.

Comparison of the various horizontal lines and line segments in Figure 19 can characterize the performance of a compensation system when the groundplane has a 1-inch deformation. Two performance measures will be addressed, the improvement in CCF produced by compensation and the deficit between an actual system and one with perfect compensation.

Improvement of CCF may be gauged by use of the horizontal line at 18 dB in Figure 19. It shows the performance of an SBR with an uncompensated 1-inch deformation of the groundplane (as shown previously in Figure 12). The distance from the horizontal segment of either curve for the compensated SBR (either of the curves labeled with a grid size) to the line for the uncompensated SBR is the gain in performance produced by the groundplane measurement system; this is more than 20 dB.

Performance deficit relative to a compensation system that produces no measurement or interpolation errors may be gauged by use of the horizontal line, labeled "DEFORMED, PERFECT MEASUREMENTS," at 51 dB in Figure 19.

The distance from the horizontal segment of either curve for the nonperfect systems to the "PERFECT MEASUREMENTS" line is the CCF deficit resulting from the residual position estimation error due to interpolation. These are 3 dB for the 9×9 grid and 10 dB for the 16×16 grid.

The two realistic systems in Figure 19 (those with measurement errors and interpolation) achieve performance comparable to the unrealistic, idealized system (with no measurement errors and no interpolation) only when two conditions are met. First, the interpolation grid size must be small enough to suppress the residual interpolation bias of position estimates. Second, the measurement errors must be small. Only then will the CCF of compensated SBRs approach that of a perfect compensation system.

The variance of the deformation estimation error $e(x,y)$, which is defined to be the difference between the estimated z coordinate $\hat{z}(x,y)$ of the groundplane and the actual z coordinate $z(x,y)$,

$$e(x,y) = \hat{z}(x,y) - z(x,y) \quad , \quad (12)$$

is shown in Figure 20. (Recall that z is normal to the undeformed groundplane.) The figure shows that the standard deviation of the position estimation error is between one and three times that of the underlying measurement error. (The quoted ratios apply only to the particular groundplane measurement-system layout in Figure 14 that was used for results presented here.)

The ratio depends on the geometry or layout of the system, i.e., where sensors and reflectors are located relative to the edges of the groundplane, and is similar to Geometric Dilution of Precision (GDOP) of the GPS system. Hereafter, the ratio will be denoted by GDOP.

As measurement error standard deviation decreases, the random part of the deformation estimation error decreases also; however, the GDOP contours shown here will be the same regardless of measurement error. Also, the average value of GDOP over the surface of the groundplane will be a constant that depends only on system layout.

In the current case, the average GDOP is 2; this means that for a given measurement error, say 0.1 in., the average deformation estimation error is 2 times the measurement error, or 0.2 inch. The estimation error is more fundamental than the measurement error, as it translates directly to a phase error. For example, a 0.1-inch RMS measurement error for compensation leads to an average RMS phase error of 7.9° ($= [0.1 \text{ GDOP}/\lambda] 360^\circ$ at $\lambda = 9$ inch, and $\text{GDOP} = 2$) because the estimation error in this case is 0.2 inch

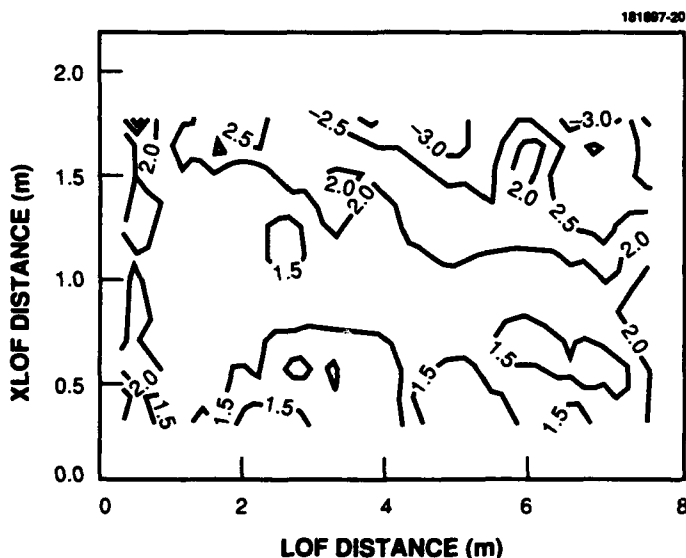


Figure 20. Contour plot of standard deviation of random estimation error normalized to measurement error (equivalent to GDOP of GPS) showing the increase in error at the edge of the antenna.

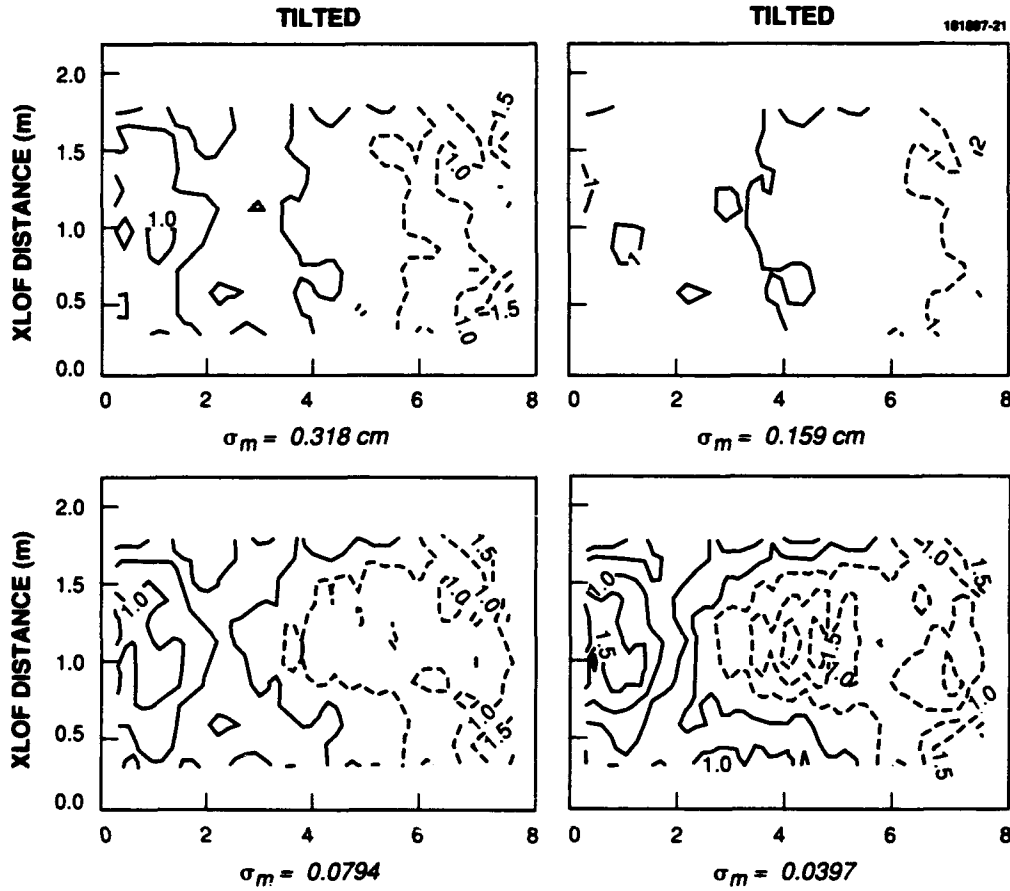


Figure 21. Contour plot of estimation-error bias normalized to measurement error showing the nature of the error with increasing measurement accuracy.

Figure 21 shows contours of the variation of residual deformation estimation error bias normalized to the standard deviation s_{MEAS} of the underlying measurement error. The bias variation $\delta\beta(x,y)$ is obtained by subtracting the average bias $\text{Ave}[\beta(x,y)]$ over the groundplane from the local bias $\beta(x,y)$ at a point

$$\delta\beta(x,y) = [\beta(x,y) - \text{Ave}[\beta(x,y)]] / s_{\text{MEAS}} \quad (13)$$

Biases are shown for four different measurement standard deviations, 0.318, 0.159, 0.0794, and 0.0397 mm. In each case the normalized residual bias lies between -2.0 and $+1.0$ regardless of the standard deviation of measurement errors. This is true for all residual biases that were examined (see Table 1).

TABLE 1
Residual Bias vs. Measurement Error

Array Size	Measurement Error Standard Deviation (cm)	Normalized Residual Bias*
16 × 16	0.3180	-1.0 to 1.5
16 × 16	0.1590	-2.0 to 1.0
16 × 16	0.0794	-1.5 to 1.0
16 × 16	0.0397	-1.5 to 1.0
9 × 9	0.3180	-0.9 to 1.2
9 × 9	0.1590	-1.0 to 1.5
* (Residual Bias)/(Measurement Error Standard Deviation)		

There is a marked change in the nature of the bias as the standard deviation of the measurement error decreases. Recall that the deformation is the same for the four different measurement standard deviations.

For measurement standard deviations 0.318 and 0.159 mm, the bias is negative (dotted contours) on the right, positive on the left, and zero (heavy solid contour) in the middle. This means that after compensating for deformation and performing linear interpolation, the antenna looks as if it is tilted slightly down on the right-hand side. As long as this apparently tilted antenna is roughly planar, the two receive radar beams will be rotated the same amount and will have the same shape, so their cross-correlation and consequent clutter cancellation via DPCA will be high.

A curious feature of the tilt is that the -1, 0, and +1 contours for the 0.318 and 0.159 mm standard deviations are at nearly the same location on the antenna's groundplane. One possible explanation for this is that the residual bias is due to nonlinear processing of measurement errors, so that on average (for the 10 realizations used for computing statistics) there is a tiltlike bias.

Recall that a nonlinear function z of a zero-mean Gaussian error γ may have a nonzero mean because to second order in the error the expected error in estimating z will be

$$\begin{aligned} E[\hat{z}(\gamma) - z(\gamma_0)] &= D_x z(\gamma_0) E[\gamma] + D_x^2 z(\gamma_0) E[\gamma^2] / 2 \\ &= D_x^2 z(\gamma_0) / 2 \{ \text{var}(\gamma) \} \end{aligned} \quad (14)$$

so

$$E[\hat{z}(x) - z(\gamma_0)] / \{ \text{var}(\gamma) \} = D_x^2 z(\gamma_0) / 2$$

where

$$D_x^n \triangleq d^n / dx^n \quad (15)$$

Thus the normalized estimation error will be independent of the standard deviation of the measurement error, as observed.

For future reference note that a rough average value of the magnitude of $D^2 \chi^2(g_0)/2$ is comparable to 1, which is the contour that lies about halfway between the right edge of the groundplane and its center (the -1 contour is similarly located on the left side of center).

As the measurement error standard deviation is decreased beyond a certain point, which appears to be between 0.159 and 0.0794 mm in this case, the residual bias due to nonlinearities will be less important than the residual bias due to interpolation errors.

The residual biases for 0.0794 and 0.0397 appear to be due to interpolation. This conclusion is supported by comparison of the contour plots for these cases with a contour plot of the deformation included in Figure 22.

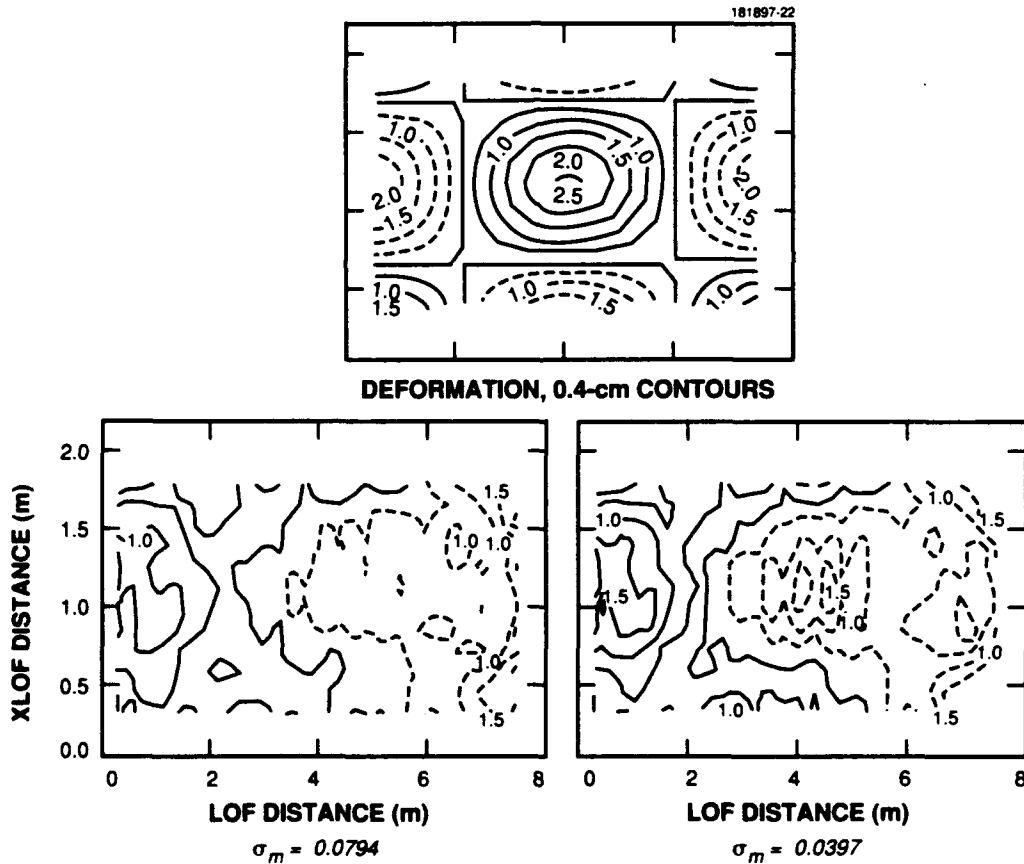


Figure 22. Contour plots showing a comparison of normalized position estimation-error bias (bottom) with the original deformation.

Note that the heavy black lines in all three plots, which are the zero contours, traverse similar paths. The hills (solid contours) produced by deformation generally correspond to valleys (dashed contours) of residual error and vice versa.

The locations on the groundplane of the -0.5 contour for the 0.0794 mm standard deviation and the -1.0 contour for the 0.0397 mm standard deviation nearly coincide; now the residual bias is independent of the measurement. For the example contours, the residual bias is -0.0397 mm regardless of the measurement error standard deviation.

The residual bias due to interpolation has maximum and minimum values of ± 0.06 mm for the 16×16 interpolation grid, so it would probably not become visible until the residual bias due to nonlinearities is about equal to this value, or until

$$D_x^2 z(\gamma_0) / 2 \{ \text{var}(\gamma) \} = 0.06 \text{ mm} \quad . \quad (16)$$

As these results indicate that $D_x^2 z(g_0)/2$ is approximately $1/1\text{mm}$ on average, the equation implies that visibility of the residual bias due to interpolation would occur when

$$\text{standard development } (\gamma) \sim 0.25 \text{ mm} \quad , \quad (17)$$

which is higher than actually occurs but is not inconsistent with the results.

Finally, all of these results are likely to be specific to the 16×16 grid. For a larger interpolation interval such as that of the 9×9 grid, interpolation errors will be larger than for the 16×16 grid; they will become visible at larger measurement error standard deviations than was the case for the 16×16 grid. The results in Figure 19 are consistent with this.

2.8 RESULTS: DYNAMIC DEFORMATION

As the physics of a dynamic system are dominated by its normal modes, it seems natural to use them as much as possible to determine the deformation of the groundplane.

To this end, the following method was devised to determine the deformed location of the antenna's radiating elements. All required measurements were assumed to be made simultaneously with a given accuracy. From these, the deformed locations of the reflectors of the compensation system were determined. (This is the same as for static deformations.)

Next, the instantaneous amplitudes $T_{m,n}(t)$ for selected modes were estimated via a least-squares procedure (Appendix C). The deformed position of a radiating element, say the i th one with undeformed coordinates x_i and y_i , was then synthesized via a truncated approximation to the full Fourier series that described the deformation;

$$z_{m,n}(x_i, y_i, t) = \sum_{0 \leq m, n \leq m_{\text{MAX}}, n_{\text{MAX}}} T_{m,n}(t) \cos(\pi m x_i / L_x) \cos(\pi n y_i / L_y) \quad . \quad (18)$$

Both $m_{\text{MAX}} < 8$ and $n_{\text{MAX}} < 8$ were varied between runs to investigate the effect of truncation of the series, which is the equivalent in this instance of interpolation grid size for the static case.

Finally, the synthesized deformed location of the radiating elements was used to phase the elements and the CCF of the antenna was computed.

Comparing the CCF obtained for two systems with different measurement errors presented a problem because, for a dynamic deformation, the CCF will vary with time similar to either of the two curves in Figure 13. For a given measurement accuracy, there is no single value of the CCF to compare with the CCF for a different measurement accuracy.

One way to characterize the performance of a compensation system with a given measurement error would be to plot curves of CCF-vs.-time for each measurement error standard deviation of interest. This curve would generally be between the "BEST" and "WORST" curves in Figure 13³. However, if many measurement errors were considered, there would be as many corresponding curves between the "BEST" and "WORST" curves; comparisons of performance would become difficult and trends that might be used to predict performance would be obscured.

To eliminate this difficulty and arrive at a single CCF for a given measurement accuracy, the performance deficit defined for a static deformation was generalized as follows. For a dynamic deformation, the performance deficit for a system with a particular measurement accuracy was defined to be the difference of subtracting the time-average CCF for that accuracy from the time-average CCF for a perfect system (that estimates all modes with no measurement error);

$$\text{Deficit} = \text{Ave}(\text{OVER TIME SERIES})[CCF_{\text{PERFECT}} - CCF_{\text{ACTUAL}}]$$

The deficit will be indicative of how far a system with a given measurement accuracy is below perfect performance, on average.

Figure 23 shows plots of deficits for three systems that make 121 measurements (using an 11×11 grid of reflectors). Each system estimates different numbers of modes. The nine-mode system estimates the three modes with lowest y spatial frequency for each of the three modes that have the lowest x spatial frequency. These modes are described by

$$0 \leq m \leq 2, 0 \leq n \leq 2 \quad (19)$$

The 12-mode system estimates the next higher x mode for each of the y modes of the previous system or estimates the additional modes described by $n = 3, 0 \leq m \leq 2$ (see Figure 24). Finally, the 16-mode system estimates the additional modes of the 12-mode system plus the next-higher y mode for each of the x modes or additional modes which are described by $m = 3, 0 \leq n \leq 3$.

The dot-dash curve shows the performance of a system that makes 64 measurements, using an 8×8 grid of reflectors, and estimates the same 16 previously described modes.

If a measurement standard deviation of 0.1 inch, or 2.5 mm, is selected, then the deficit is 12–16 dB, compared to a worst case of about 8 dB for the static deformation described earlier. The time-average best CCF is 56 dB, so the time-average CCF for a compensation system with measurement accuracy of 0.1 inch is $(56 - 16 =) 40$ to 44 dB. This is comparable to the CCF for a static deformation compensation system that uses a 9×9 grid (see Figure 12).

³ Although not shown here, this has been confirmed to be the case.

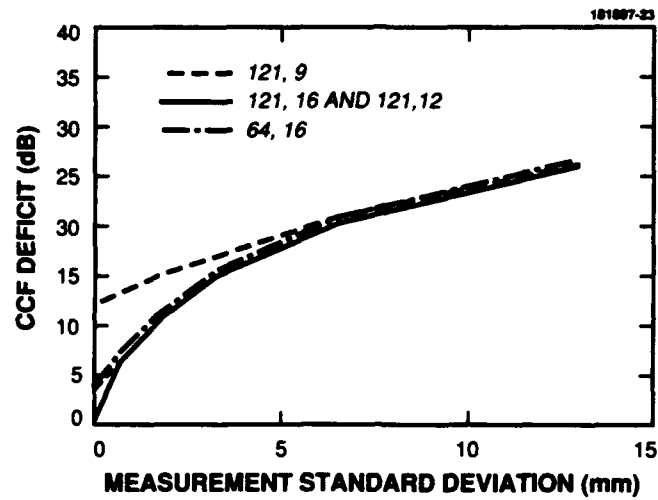


Figure 23. CCF deficit (defined in text) vs. measurement accuracy for various numbers of measurements and estimated modes.

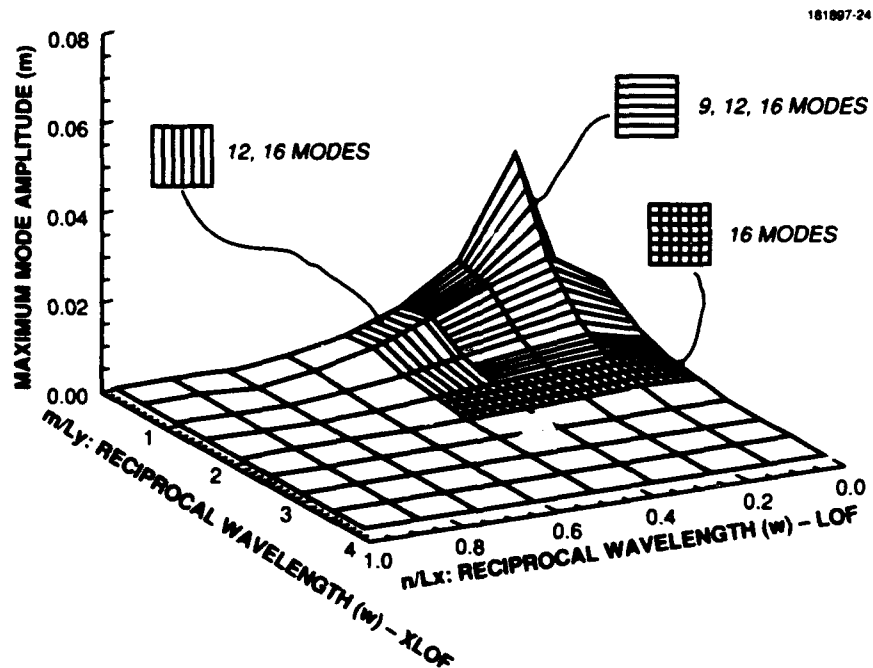


Figure 24. Fourier space plot of maximum deformation amplitudes showing the particular modes that were estimated in each case in Figure 23.

2.9 TIMELINE PROBLEMS FOR VIBRATIONS

The assumption that all measurements were made simultaneously, which was made to allow a simple feasibility demonstration of estimation of mode amplitudes, is unrealistic. Any laser-based deformation compensation system will almost certainly make serial, or round-robin, measurements. This presents a problem, as the following demonstration shows.

The collage shown in Figure 25 comprises snapshots of deformations taken at times ranging from 0.25–1.25 seconds, in 0.25 second increments. Suppose that the groundplane is covered by an 11×11 grid (not shown) of reflectors and that their positions are measured one after the other, beginning in the lower right corner of the antenna (as seen in these pictures) and progressing along a row from front to back, then beginning in the next row to the left and progressing again from front to back, etc., proceeding by rows from right to left until the positions of all sensors have been estimated.

If the dwell at each reflector is 10 msec, at the time indicated below each frame the three sensors will be obtaining a sample at the position indicated by the dot in the frame.

The composite deformations that are estimated using the data from a serial sampling scheme will obviously not look like any one snapshot of the deformations, hence the deformations will not be valid for any time in the sampling interval. The deformation will be skewed by the sampling method.

Table 2 indicates changes that one might make to reduce the sampling interval, which will be called the frame time hereafter.

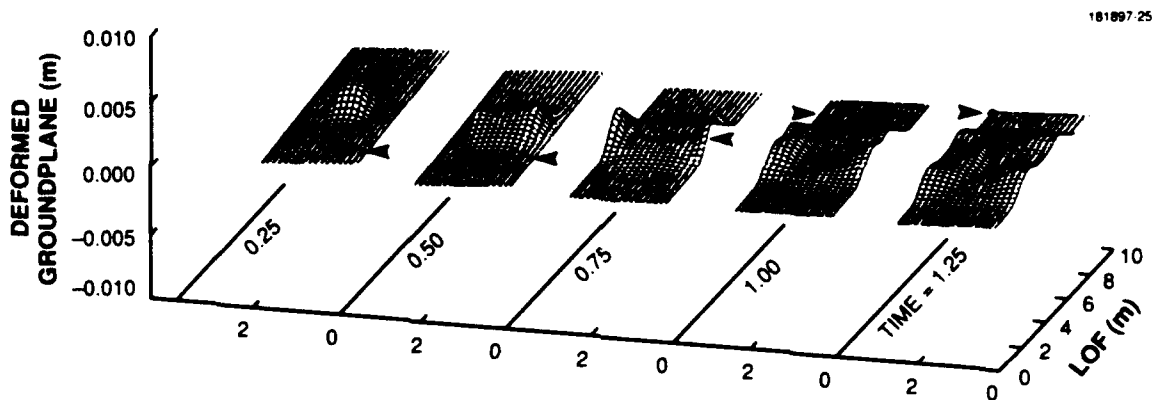


Figure 25. Evolution of deformation showing location of measurement, for a serial measurement scheme, at indicated times; 121 points are measured with a dwell time of 10 msec per point.

TABLE 2
Changes That Reduce Frame Time (Skew)

Element	Change	Frame Time (sec)
Reflectors*	121 -> 64	0.64
Dwell Time (sec)	0.01 -> 0.002	0.24
Both	(Above)	0.128
* This reduction is only feasible if modes are estimated.		

Two msec is near the minimum time required for the laser's beam director to slew to the general area in which a reflector will occur, localize it, and make a measurement of distance. Figure 23 shows that 64 is the smallest number of reflectors that produces acceptable CCF deficits, so this was assumed to be the lower limit for Table 1; in addition, experience to date has shown that it is impossible to estimate 16 modes with fewer reflectors.

Experience to date (trial and error) has shown that the minimum number of reflectors arrayed on a rectangular grid that yields accurate estimates of 16 modes is at least 64 ($= 8 \times 8$). This happens because the matrix $H H^T$ that occurs in least-squares estimation⁴ is singular if less than 64 measurements are attempted⁵ (at least for rectangular and other grid geometries that have been tested).

If both of the indicated reductions could be made, it is still unlikely that a 50-dB CCF could be achieved. If it cannot be achieved, a processing scheme that predicts deformations will be required.

2.10 SERIAL MEASUREMENTS AND PREDICTION

For the deformation problem at hand, two prediction methods come to mind. Either the position of each reflector (64 positions in all) or the amplitudes of modes (16 modes) could be predicted.

⁴ $\underline{z} = H\underline{x}$, solved via least squares yields $\underline{x} = (HH^T)^{-1} H\underline{z}$.

⁵ These frustrating results can be rationalized (though not yet proved) as follows: to obtain a four-element FFT requires a set of eight real samples. For a rectangular grid, this is true for each dimension; to obtain a two-dimensional 4×4 FFT requires an 8×8 set of real samples. The least-squares procedure estimates bias and slope in two dimensions as well as the 16 magnitudes of the selected modes. Thus, in addition to producing other estimates, the least-squares procedure is essentially performing a 2-D FFT, so the above constraint on FFTs must hold in this case.

One consideration in deciding which method to use is that the time dependence of the modes is known if a good structural model of the antenna is available. Further, the model time dependence of a mode is easily described in terms of a differential equation or a state-transition matrix. This is not the case for the prediction of the displacement of a reflector.

Another factor is the revisit rate, which for 64 reflectors is on the order of 0.1 sec. This factor is dealt with in some detail in the following comparison of the two prediction methods.

2.10.1 Prediction of a Reflector's Location

If prediction of a reflector's location is attempted, the overall strategy would be to predict the location of each of the reflectors in an $N \times N$ array based on a sequence of measurements of the reflector's previous position. The measurements and predictions would be for a given reflector, and only measurements for that reflector would be used to predict its position. Reflectors would be processed serially.

A diagram of the timeline for this process is shown in Figure 26. The measurement time for any reflector would be the dwell time, 2 msec in the example; the latest measurement for the reflector would be incorporated via a filter to update the estimate of the reflector's current position. Until the next measurement update (which is 240 msec later for an 11×11 grid of reflectors), the position would be predicted. The long prediction interval compared to the mode frequencies, which are below 7 Hz, can be expected to produce poor predictions.

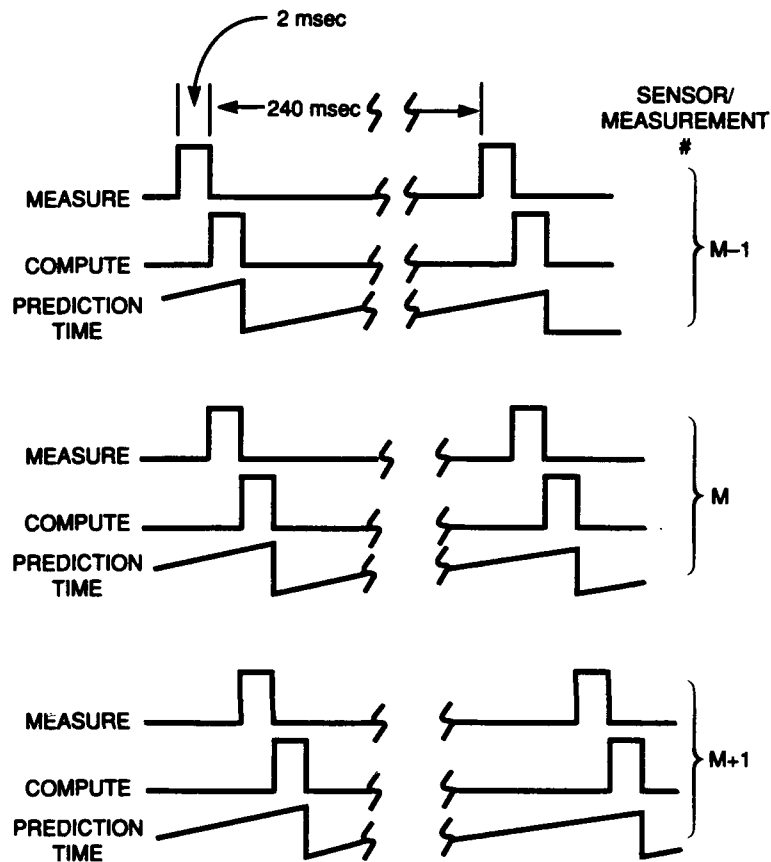
This method is cumbersome and requires a great deal of memory; results shown in Figure 25 indicate that each reflector's position would be described by about 12 modes, each oscillating at different frequencies, so a filter would need a state vector for each mode. If there were 121 reflectors, the memory and number of computations would be very large.

2.10.2 Prediction of a Mode's Amplitude

As in the previous discussion, measurements are of the deformations of the reflectors and require 2 msec. The measurements, however (see Figure 27), are incorporated into estimates of the mode amplitudes that are produced by a filter; about 12 modes are estimated. Every measurement is used to update the estimates, so the maximum staleness of an estimate is 6 msec compared to 240 msec for prediction of measurements.

Also, modes are predicted on demand for times between updates, so the maximum prediction interval is about 10 msec, much shorter than that for prediction of measurements. Consequently, the predictions for this method should be more accurate than for the one involving prediction of measurements.

Figure 28 shows a schematic computation flow diagram for a canonical method of estimating and predicting mode amplitudes and synthesizing deformations from them. The flow is from measurements at left, to prediction of mode amplitudes as required, and finally to synthesized deformations at right.



NOTES

DIGITAL SIGNALS MEASURE & COMPUTE

ANALOG SIGNAL PREDICTION TIME

MEASURE = DETERMINE 3 LENGTHS @ 2 msec EA.

TOTAL MEASUREMENTS = $3 \times 11 \times 11$

Figure 26. Timelines for prediction of location of each reflector, or measurement grid point, showing sequence of measure, compute, predict for three sequential measurements.

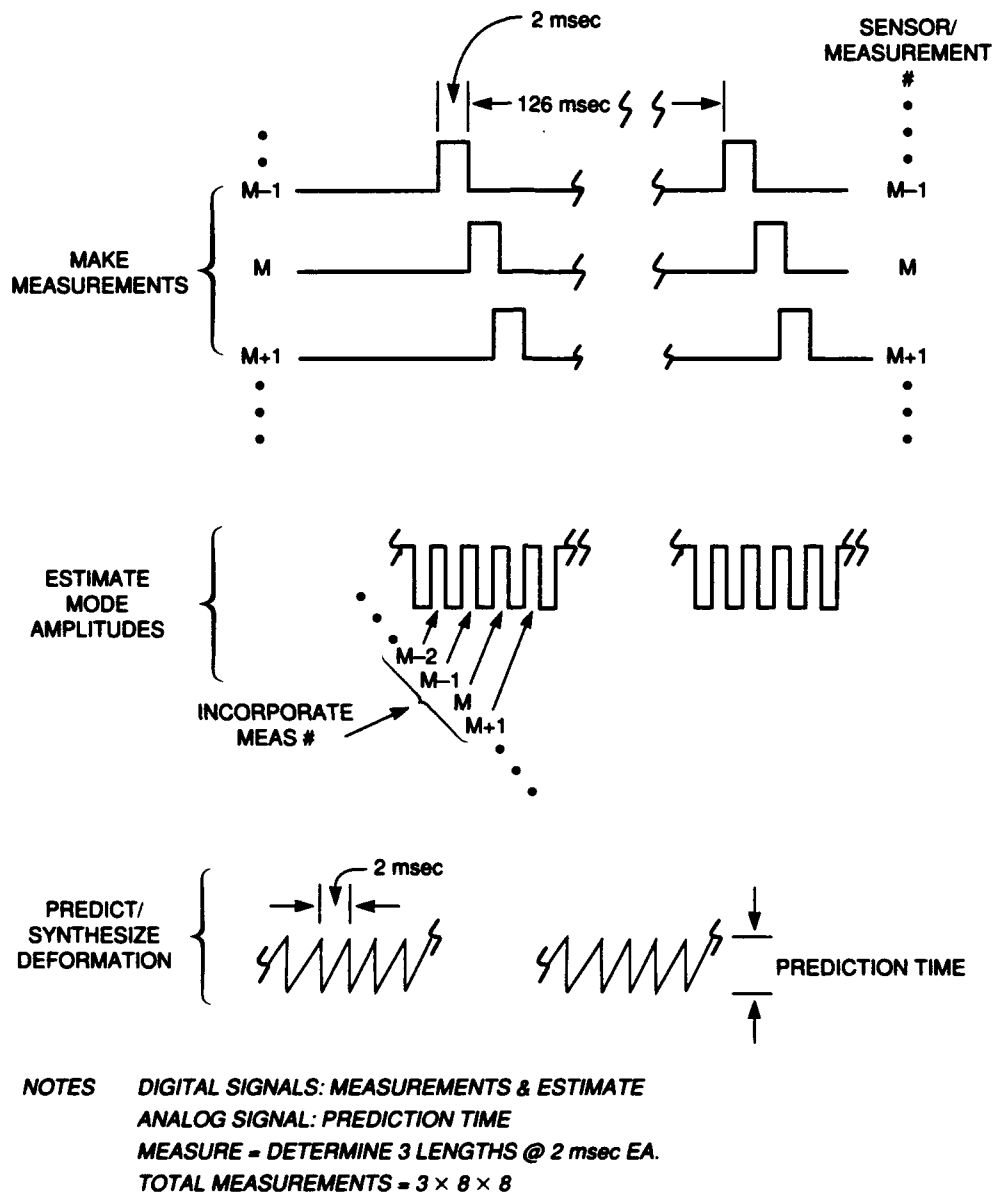


Figure 27. Timelines for synthesis of location of each reflector, or measurement grid point, showing sequence of (three) sequential measurements, estimation and prediction of mode amplitude, and synthesis of deformation.

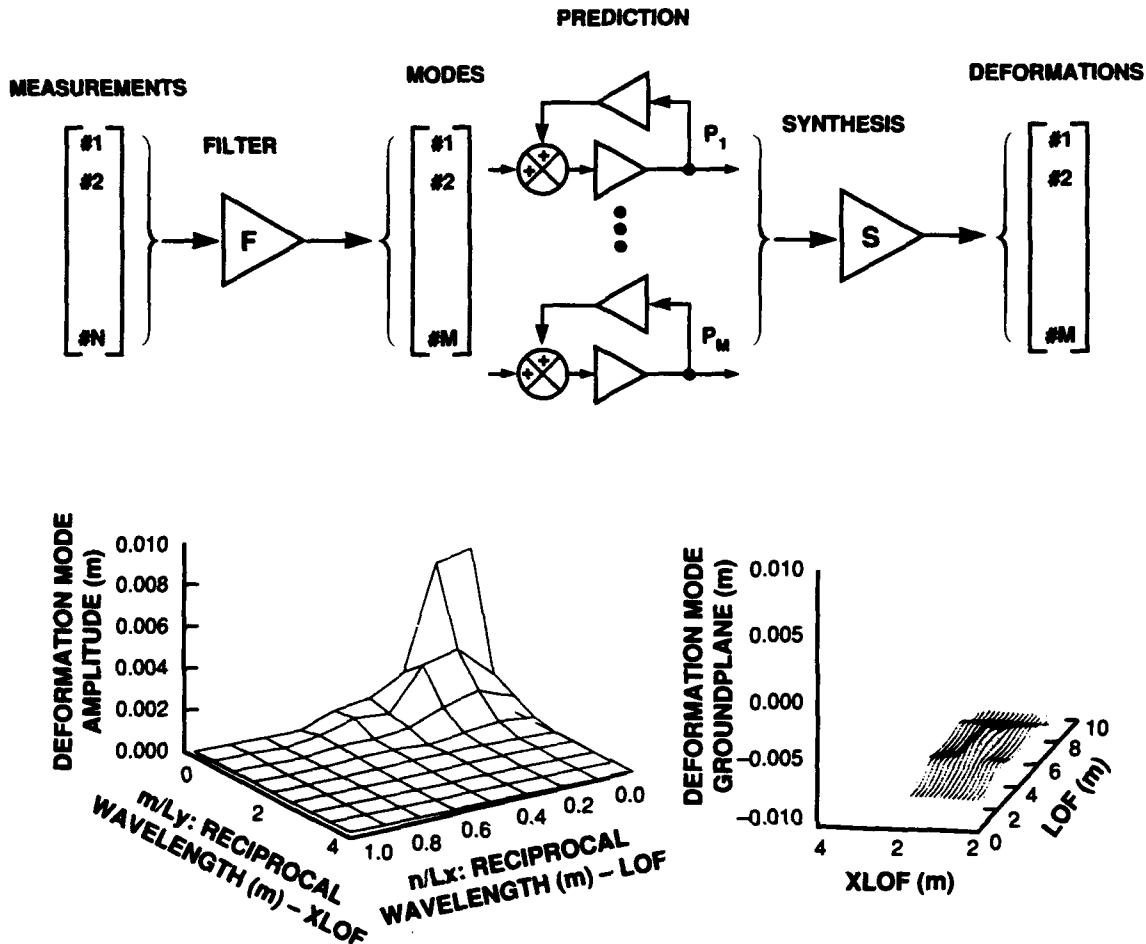


Figure 28. Canonical computation flow diagram for prediction and synthesis of deformation modes.

For the situations described thus far, the number of measurements, N , will be between 64 and 121; the number of modes, M , between 9 and 16; and the number of deformations, J , much larger than either ($J = 576$, 12 rows of 48 radiating elements each, for the SBR model antenna used here). All deformation information resides in the modes, which constitute the smallest set of the three and are the most easily modeled and predicted.

There was not enough time to design and model a Kalman filter to simulate the procedures depicted in Figure 28, yet it was desirable to demonstrate the possibility of predicting modes.

A credible demonstration would require that modes be estimated from noisy measurements. This would provide a method of simulating — rather than guessing — the approximate amplitudes of mode-estimation errors. The demonstration would also require that elements of the mode state vector be estimated from the estimates of mode amplitude. The efficacy of mode prediction could then be demonstrated by comparing the predicted mode amplitudes vs. their actual values.

To achieve the desired results, a demonstration with the following elements was devised.

Estimation of Mode Amplitudes. Because a least-squares method existed for estimating mode amplitudes from a number of simultaneous measurements ("snapshots") of the deformed groundplane, this apparatus was used. With it, estimates of mode amplitudes were obtained from multilateration using noisy measurements. This was performed for snapshots of the deformed surface at two different times. The result was a reasonably credible set of estimation errors for mode amplitudes, as desired.

Estimation of State Vector Components. Each mode is effectively a damped oscillator whose decay time and frequency are known, so the state transition matrix can be computed regardless of measurements. The state vector will have two components corresponding to the amplitude of a damped cosine and a damped sine wave. Given mode amplitude estimates at two different times, the two components at either of the measurement times can be computed with the aid of the state transition matrix.

Note that if the mode estimates are in error, as they surely will be, the two components will also be in error. Because the number of mode estimates is equal to the number of components, the resulting estimation error for the components of the state vector will be larger than for situations where a suitable algorithm is employed to obtain two components from greater-than-two-mode estimates. For a given set of mode amplitudes, the technique for estimating components is a worst-case procedure; one might do better with more amplitude estimates and another algorithm for estimating components.

Prediction of Mode Amplitudes. After the state vector for the second measurement time was estimated, predictions of the state vector were made by propagating the estimated state vector to the required time via the propagation matrix. The predicted and known (from the deformation model) mode amplitudes could then be compared.

2.11 PREDICTION RESULTS

Figures 29 and 30 show the successes and failures at predicting 12- or 16-mode amplitudes by the described methods. As shown in Figure 29, prediction of the $(n,m) = (1,0)$ mode is reasonably accurate. The solid curve in the figure is a time history of the actual amplitude. The dot-dash curve is a time series of the amplitude estimated from snapshots of the deformation, as described previously. The + signs are elements of the time series of predicted amplitudes.

In this and all other figures, the first two + signs are forced to lie on the dot-dash curve by the fitting procedure that determines the initial components of the state vector of the mode. All subsequent + signs are predicted from the first two, while the remaining points on the dot-dash curve are obtained from a set of simultaneous measurements made each time the deformation is sampled. The solid curve is used to calculate the deformation to be sampled.

The vertical distance between the solid and dot-dash curves is the estimation error. If no error occurs, then the two curves coincide; if they are far apart, the error is large. Similarly, the vertical distance from a + sign to the solid curve is the prediction error of the mode amplitude.

Note that the success of the prediction of the $(1,0)$ amplitude can be attributed to the near coincidence of the solid and dot-dash curves for the first two points; in other words, to the very small mode-amplitude-estimation error in this case. Also note that even though the estimation error for the first two points is invisible to the eye, it still produces significant errors at later times.

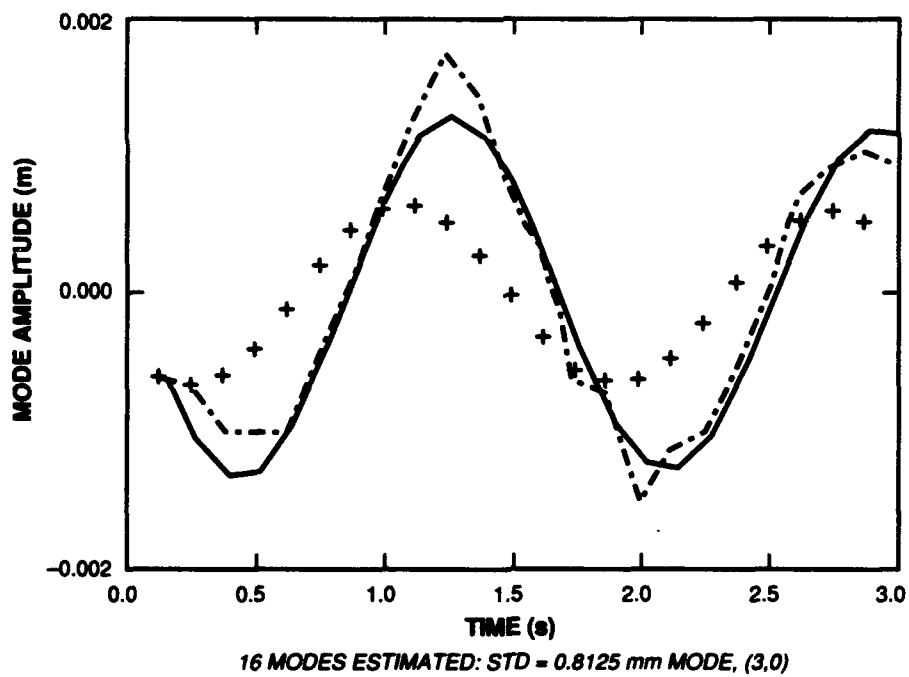
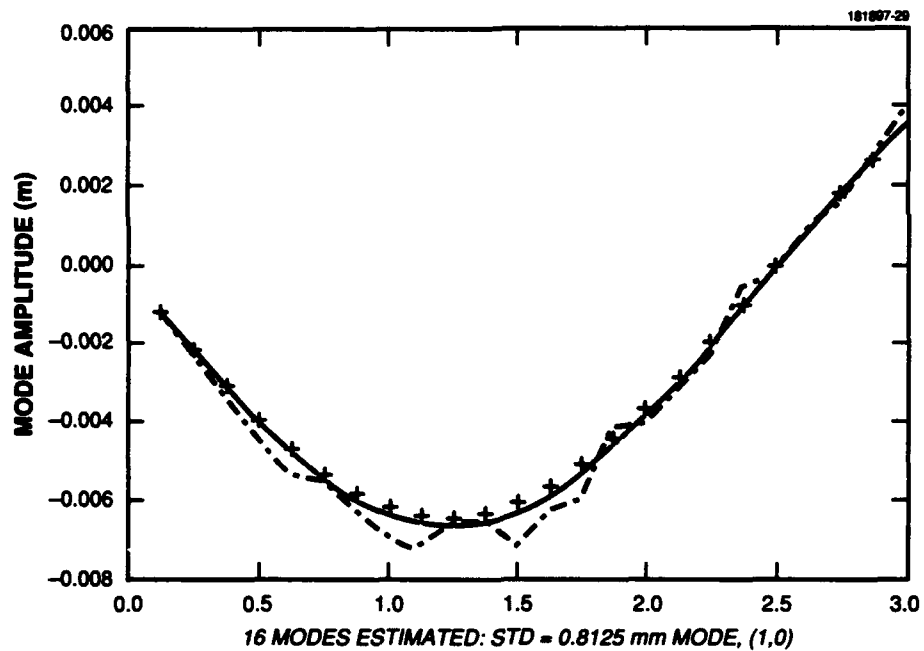


Figure 29. Plots of actual (solid curve), measured (dot-dash curve), and predicted (+'s) mode amplitudes.

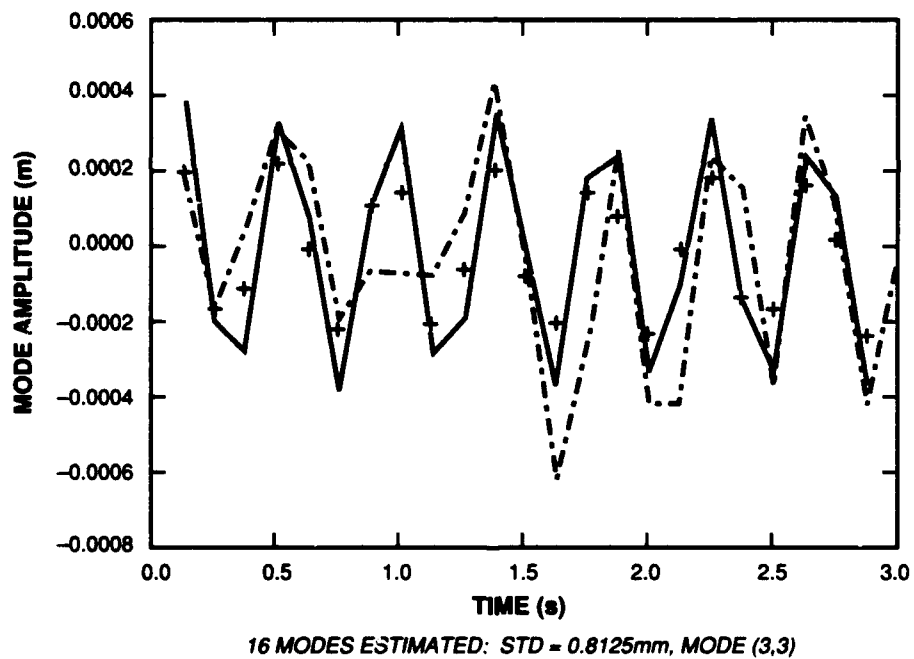
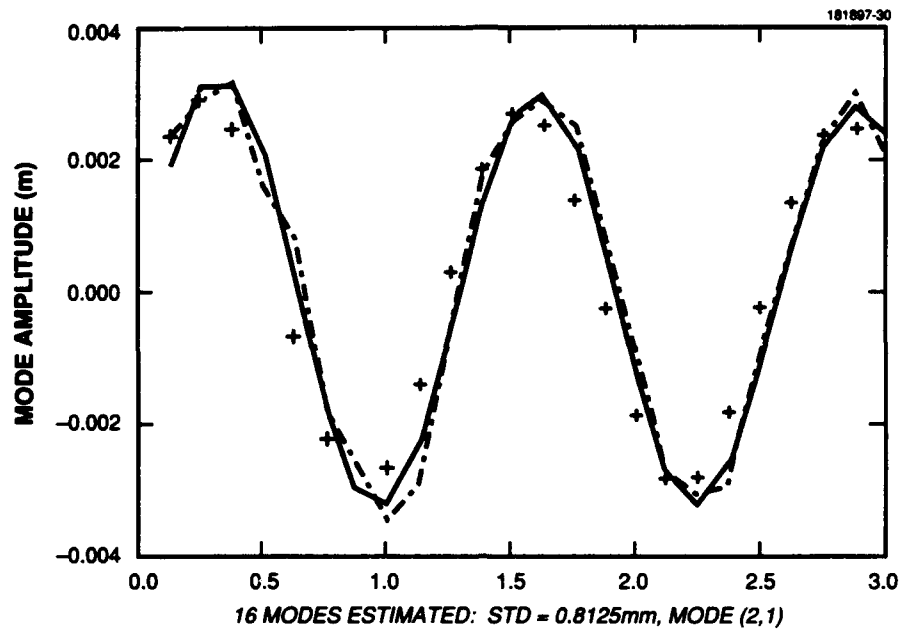


Figure 30. Plots of actual (solid curve), measured (dot-dash curve), and predicted (+'s) mode amplitudes.

The prediction results for mode (3,0) are among the worst failures in the set of 16 modes that was estimated. The cause of the failure is the large estimation error (vertical distance between the solid and dot-dash curves) for the second fitting point. As a result, both amplitude and phase of the prediction are in error.

The top part of Figure 30 shows the efficacy of predicting modes. Recall that the prediction, which spans two periods of the oscillation of the mode amplitude, was made using the first two points, which are one tenth of a period apart. This is possible because the mode's frequency and decay constant are known, so the propagation matrix can be accurately computed. The propagation matrix produces the damped oscillation. The amplitude and phase are determined by the components of the state vector.

The phase and amplitude errors of the prediction relative to the actual mode amplitude are moderate, but the prediction maintains its accuracy over the interval of time spanned by the plot.

Results for the highest frequency mode, (3,3), are also shown in Figure 30. The zero-to-peak mode amplitude is about 0.004 m; judging by the vertical distance between the solid and dot-dash curves, the mode amplitude is probably less than 10 times larger than the standard deviation of the estimation error.

One might expect the prediction errors to be large, as they are, but the predictions (+) and measurements (dot-dash curve) are of comparable accuracy. This is significant considering that far fewer calculations are required to predict than to estimate the mode amplitude from a set of measurements.

The average-over-time of the ratio of the actual mode amplitude to the estimation error (Figure 31) is between -1 and 22 dB; for half of the estimated modes the ratio is above 8 dB.

In summary, the demonstration indicates that modes can be predicted with modest accuracy using the simplest conceivable algorithm. A more sophisticated procedure could improve the prediction accuracy so that prediction could be used if required, as it likely would be.

The prediction results for mode (3,0) are among the worst failures in the set of 16 modes that was estimated. The cause of the failure is the large estimation error (vertical distance between the solid and dot-dash curves) for the second fitting point. As a result, both amplitude and phase of the prediction are in error.

The top part of Figure 30 shows the efficacy of predicting modes. Recall that the prediction, which spans two periods of the oscillation of the mode amplitude, was made using the first two points, which are one tenth of a period apart. This is possible because the mode's frequency and decay constant are known, so the propagation matrix can be accurately computed. The propagation matrix produces the damped oscillation. The amplitude and phase are determined by the components of the state vector.

The phase and amplitude errors of the prediction relative to the actual mode amplitude are moderate, but the prediction maintains its accuracy over the interval of time spanned by the plot.

Results for the highest frequency mode, (3,3), are also shown in Figure 30. The zero-to-peak mode amplitude is about 0.004 m; judging by the vertical distance between the solid and dot-dash curves, the mode amplitude is probably less than 10 times larger than the standard deviation of the estimation error.

One might expect the prediction errors to be large, as they are, but the predictions (+) and measurements (dot-dash curve) are of comparable accuracy. This is significant considering that far fewer calculations are required to predict than to estimate the mode amplitude from a set of measurements.

The average-over-time of the ratio of the actual mode amplitude to the estimation error (Figure 31) is between -1 and 22 dB; for half of the estimated modes the ratio is above 8 dB.

In summary, the demonstration indicates that modes can be predicted with modest accuracy using the simplest conceivable algorithm. A more sophisticated procedure could improve the prediction accuracy so that prediction could be used if required, as it likely would be.

3. SUMMARY, CRITIQUE, AND UNFINISHED WORK

The work described herein is unfinished. The following has been accomplished:

Multilateration, a method of compensating for deformations of a large array, was identified and its efficacy for a radar that uses DPCA was evaluated using the clutter-cancellation factor. The result was that clutter cancellation could be improved by about 20 dB for the particular radar and deformations that were used. To achieve this cancellation for deformations whose zero-to-peak magnitude was 1 inch required between 100 and 200 measurements with accuracies of 0.1 inch, which is about 1 percent of the 10-inch wavelength of the radar.

In general, improvement in clutter cancellation will depend on the magnitude and shape of the deformations, the type of measurements that are made (multilateration vs. triangulation — see the later discussion in this summary), and the layout of the elements of the system; the specific numbers given in the previous paragraph almost certainly will not apply to other situations. What is important is the demonstration that measurement of deformations of a radar antenna and appropriate compensation of the phase of its radiating elements produces significant improvement in clutter cancellation for DPCA.

Similarly, the model of deformations used here, although bearing a passing resemblance to predicted deformations of an actual radar design, will probably not be encountered in other radar designs. What is important here is that a knowledge of a few of the significant deformation modes of the structure allows the deformations to be synthesized with enough accuracy to produce significant improvement in clutter cancellation. The number of modes required to describe a fairly complicated deformation is surprisingly small.

The significance of a modal description of a structure is twofold. First, it allows the location of the radiating elements tied to the structure to be synthesized without interpolation between a fixed grid of points on the structure. This has the potential of requiring fewer measurements than interpolation would, especially if the deformations are characterized by a few modes with short characteristic periodic lengths.

Second, and most important for a live structure which has time-varying deformations, the amplitude of the normal modes are the physical entities that are excited by forces applied to the structure; modern, sophisticated deformation prediction techniques, which are based on the physics of normal modes, use simple second-order differential equations to describe the dynamic deformation of the structure. This means that a Kalman filter can be formulated whose state-vector components are a normal mode's amplitude and rate; one two-state filter would be required for each mode. The filter's dynamics matrix will comprise the constants for the second-order differential equations of the mode. The physical plant noise of the filter will be the appropriate coefficient of the modal decomposition of the random, unknown forces that act on the structure. The deformations may then be synthesized — and perhaps more important — reliably predicted from the elements of the set of state vectors used to describe the deformation.

This last assertion about prediction of modes was investigated here using a crude technique to estimate mode amplitudes. The results obtained for prediction of mode amplitudes demonstrated the ability to predict well enough to offer possibility of improved prediction accuracy when more sophisticated techniques are used.

The implementation of a laser-based system to perform measurements for multilateration was a reasonable first choice for an active measurement system. However, in retrospect, a better choice might have been to use the technique, described by Attia [2], of cross correlating clutter returns of pairs of radiating elements. However, instead of rephasing the radiating elements for each look direction of the radar, as proposed by Attia, the returns from three separate patches of clutter should be used to determine the deformation of the antenna. The clutter returns would have to be from widely separated look directions so that the angles between the look directions from the radar to the clutter patches were large and not coplanar. These constraints reduce the geometric pattern of random-estimation error in the antenna's nominal plane that will be produced by this technique. The origin of the pattern is analogous to the origin of GDOP for the GPS satellite system, and the pattern itself is analogous to the pattern of random errors shown in Figure 20.

Estimating deformations rather than rephasing each element will allow a small subset of the radiating elements to be cross correlated, thereby cutting down the processing load; estimating the deformations will again allow the estimation and prediction of deformation-mode amplitudes that were described earlier. Measurement of deformation via clutter returns coupled with Kalman-filter estimation of selected mode amplitudes should yield an accurate, computationally efficient (compared to rephasing all radiating elements for each look direction) method of improving clutter cancellation in the presence of deformations.

There is an opportunity for more investigation along these lines. This must be left to a future date and perhaps to another investigator.

APPENDIX A CLUTTER CANCELLATION

The performance measure for deformation compensation used throughout this work is the clutter cancellation factor (CCF), which is a measure of the cross correlation, integrating over all space, of the radar's two receive beams weighted by its transmit beam [7]. CCF is a measure of residual clutter power after DPCA processing relative to raw clutter power.

If the element pattern is assumed to be unaffected by deformations (i.e., not tilted away from normal to the plane of the undeformed antenna), the CCF is usually approximated by this sequence of calculations (which parallels the flow shown in Figure 3 of the main text):

First, the electric field patterns $E^j(q)$, where $j = 1, 2$ designates the leading and trailing receive apertures, respectively, are calculated;

$$E^j(\theta) = \gamma_{\text{ELEM}}(\theta) \sum_{n=1}^{N_{\text{ELEM}}} W_n \exp(i\Delta\phi_n) \quad (20)$$

Here, $E^j(q)$ is the array factor multiplied by the element pattern $\gamma_{\text{ELEM}}(\theta)$; w_n is the element weight, which for the calculations summarized here is a particular version of a raised cosine weight developed by R. Miller for a demonstration model of an SBR [14], and where the phase of each element

$$\Delta\phi_n = (\underline{k} - \underline{k}_0) \cdot (x_n - x_{\text{AVE}}) \quad (21)$$

is computed relative to the location of the average phase center, x_{AVE} , which is assumed to be at the geometric center of the aperture [7],

$$x_{\text{AVE}} = \frac{1}{N_{\text{ELEM}}} \sum_{n=1}^{N_{\text{ELEM}}} x_n \quad (22)$$

and the steered wavevector is

$$\underline{k}_0^T = 2\pi [\sin(\theta_0)\cos(\phi_0), \sin(\theta_0)\sin(\phi_0), \cos(\theta_0)] / \lambda \quad (23)$$

where θ_0 and ϕ_0 are the steered scan and azimuth angles, respectively, and λ is the radar wavelength.

The cross-correlation product M_{12} of the electric fields of the two receive apertures is then calculated using, as a correlation weight, W_m , the squared magnitude of the transmit electric-field pattern $E^T(\theta)$, which is computed as described previously except that the range of the sum is over the transmit aperture and the elements are uniformly weighted ($w_n = 1$). The magnitudes of the two receive beams M_{11} and M_{22} are also calculated so that a correlation coefficient may be computed later;

$$M_{12} = \sum_{m=-M}^M W_m E^1(\theta_m) E^2(\theta_m)^* \quad (24)$$

and

$$M_{jj} = \sum_{m=-M}^M W_m |E^j(\theta_m)|^2, \quad j=1,2, \quad (25)$$

where * denotes complex conjugation and the correlation weight W_m is

$$W_m = |E^T(\theta_m)|^2. \quad (26)$$

Instead of integrating the two receive beams over all space to obtain the cross correlation, they are instead summed over a range of angles:

$$\theta_m = \theta_0 + m\delta\theta \quad |m| = 0, 1, \dots, M-1, M, \quad (27)$$

where θ_0 is the steering angle, the radar's azimuth angle is 0, $\phi_0 = 0$, and, the steered wavevector⁶ is

$$\underline{k}_0^T = 2\pi [\sin(\theta_0), 0, \cos(\theta_0)] / \lambda. \quad (28)$$

In all CCF calculations performed here the radar was assumed to be aimed at an angle $\theta_0 = 30^\circ$ from broadside at zero azimuth angle relative to the line of flight of the radar, which corresponds to $\phi = 0$.

The one-dimensional sum has been found to produce nearly the same CCF as a two-dimensional integral over all angles θ and ϕ [7]. The integer M that determines the number of samples summed is determined by a test of convergence of CCF to a stable result.

Finally, the magnitude of the cross correlation is squared, normalized by the product of the magnitude of the two receive beams, subtracted from one, and expressed in decibels:

$$CCF = -10 \log [1 - |M_{12}|^2 / (M_{11}M_{12})] \quad (29)$$

The two receive apertures of an undeformed groundplane will have a cross correlation equal to 1 and, consequently, will produce an infinite CCF. Clutter will be completely cancelled in this case. In contrast, deformations that completely decorrelate the two receive apertures will have no cross correlation (i.e., the result is zero), so the CCF will be 0 and residual clutter will be high.

⁶ See Section 2.2, "Algorithm for steering the antenna."

APPENDIX B DEFORMATIONS

Investigating the effectiveness of compensating for deformations requires a model of the SBR's structure. As a detailed SBR design is not available, a simple model that includes relevant features of the motion of structures must suffice. The main feature required of the model is that it have deformation modes.

Here, the antenna groundplane of the SBR will be modeled as a rectangular thin membrane that is the two-dimensional analog of the stretched string [15]. In this model, the membrane at rest is in the x,y plane and is constrained to move perpendicular to the plane so that $z(x,y,t)$ is the displacement of the membrane at the point whose coordinates are x,y . The velocity of the membrane at this point is the partial derivative of z with respect to time, t .

In addition to the usual net restoring force per unit area [19],

$$F_{\text{RESTORE}} = \alpha \left(\frac{\delta^2 z}{\delta x^2} + \frac{\delta^2 z}{\delta y^2} \right) \quad , \quad (30)$$

where the restoring constant is α ; a damping force per unit area will be added to the equation of motion. Damping is presumed to be proportional to the velocity of the membrane, and the proportionality constant v will be presumed to be independent of any mode:

$$F_{\text{DAMP}} = -v \frac{\delta z}{\delta t} \quad . \quad (31)$$

An external force $f(x,y,t)$ can presumably be applied to the structure (by thrusters or thermal gradients). Consequently, the net force, or sum of these three forces, will equal the acceleration. The equality leads to a second order partial differential equation:

$$\frac{1}{c^2} \frac{\delta^2 z}{\delta t^2} + \frac{v}{\alpha} \frac{\delta z}{\delta t} - \left(\frac{\delta^2 z}{\delta x^2} + \frac{\delta^2 z}{\delta y^2} \right) = \frac{f(x,y,z)}{\alpha} \quad , \quad (32)$$

where, for a membrane with mass density ρ , the speed of the deformation wave c , and characteristic damping time θ , will be

$$\begin{aligned} c &= (\alpha / \rho)^{1/2} \\ \theta &= 2\rho / v \end{aligned} \quad . \quad (33)$$

The rather simple model used here has led to a single second-order partial differential equation that has more than superficial similarity to sets of ordinary differential equations (ODEs) derived from more detailed and complicated analyses of structures using finite element models. Such models yield a set of second-order coupled ODEs that describe the motions of elements, trusses, plates, etc., of the structure. The set of coupled ODEs has solutions that are normal modes which correspond to the eigenfunction solutions of the above partial differential equation (PDE). The PDE is a convenient way to obtain models of the normal modes of the groundplane.

By choice of the analyst, the finite element model and the resulting ODEs may at first contain only the restoring, forcing, and inertia terms. (The inertia term involves the second derivative of time and is a result of Newton's second law.)

Damping of the structure, which is usually the hardest element to model, is then added by assuming that it is either modal (which requires a different damping constant for each mode) or has some other interesting property.

The particulars of the damping model will affect the resonant or mode frequencies so that they are different for the damped and undamped structures. Attempts have been made to adjust the damping to change the frequencies of the undamped model so that they coincide with measured frequencies for the modeled structure.

Regardless of the way it is modeled, damping of a structure is a very real feature — structures don't vibrate forever. Damping was included in the deformation model to provide verisimilitude and to include an important feature required for constructing Kalman or other filters needed to accurately predict vibrations.

In summary, the derivation of the above PDE, the nature of the various terms it contains, and the results it produces are not unlike corresponding aspects of a finite element analysis of a more complicated SBR. In addition, the PDE has the added feature of ease of construction and general convenience for the problem at hand.

The boundary conditions for the problem are that the edges of the antenna are free to move; the slope at right angles to the edge is zero at the edge. At the edges at $x = 0$ and $x = -L_x/2$ one may write these equations:

$$\frac{\delta z}{\delta x}(0, y, t) = 0 \quad \frac{\delta z}{\delta x}(l_x, y, t) = 0 \quad (34)$$

These are in contrast to the usual conditions on a vibrating membrane, where the edges are clamped in a rigid frame.

Two different situations were used to illustrate properties of a deformation-compensation system. First, a static case (all time-partial derivatives equal to zero) was used to examine measurement accuracies required to support 20–50 dB of clutter cancellation. The response to an impulse applied to a given area of the antenna was then investigated to illustrate problems that arise in the actual working environment of a compensation system. For the static case, the deformation was assumed to be

$$z(x, y) = A \cos(2\pi x / L_x) \cos(2\pi y / L_y) \quad (35)$$

This can only be achieved if the force $f(x, y)$ on the antenna's groundplane (which is presumably due to a fictitious thermal gradient) is

$$f(x, y) = -(2\pi)^2 \alpha z(x, y) (L_x^{-2} L_y^{-2}) \quad (36)$$

This particular deformation has the spatial variation of one of the eigenfunctions of the full time-dependent equation. However, in contrast to that eigenfunction, this deformation is not a function of time.

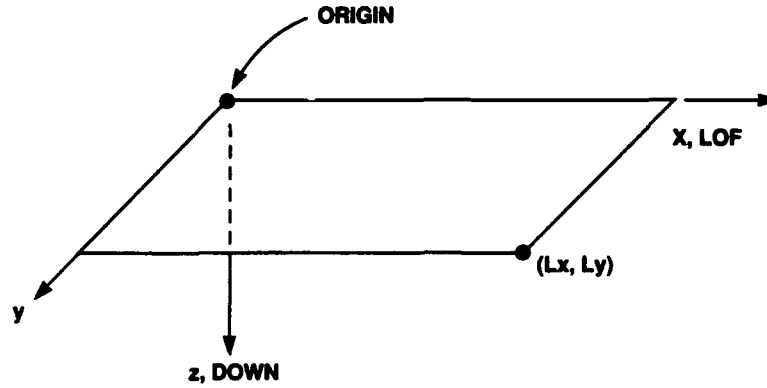


Figure B-1. Radar antenna groundplane (membrane) coordinate system.

If the dynamic case is considered, the full equation must be solved, which is easily done by separation of variables to obtain a set of orthonormal functions used to obtain a Fourier-series representation of the force. This representation then results in a second-order ODE with a forcing function, which in turn is easily solved.

Suppose that in the coordinate system (shown in Figure B-1) eigenfunctions $e_{m,n}$ are assumed to have the form

$$e_{m,n}(x, y) = \cos(\pi n x / L_x) \cos(\pi m y / L_y) T_{m,n}(t) \quad , \quad (37)$$

where m and n are non-negative integers. These satisfy the boundary conditions at all times.

Further, write the force as a Fourier series⁷:

$$\frac{f(x, y)}{\alpha} = \sum_{m,n} \frac{f_{m,n}}{\alpha} \cos(\pi n x / L_x) \cos(\pi m y / L_y) \delta(t) \quad . \quad (38)$$

Substitution of these into the equation yields a simple ODE for $T_{m,n}(t)$:

$$\ddot{T}_{m,n} + c\mu\dot{T}_{m,n} + (k_{m,n} - c)^2 T_{m,n} = f_{m,n} \delta(t) \frac{c^2}{\alpha} \quad , \quad (39)$$

where a dot denotes differentiation with respect to time,

$$k_{m,n} = (2\pi) \{(m / L_y)^2 + (n / L_x)^2\}^{1/2} \quad (40)$$

⁷ If the coordinate system origin is shifted to $x = L_x/2$, $y = L_y/2$, the series of cosines becomes the usual Fourier series of sines and cosines, so the expansion is possible.

and

$$\mu = \frac{vc}{\alpha} \quad (41)$$

There are three solutions to this equation; one each for $k_{m,n} > \mu/2$, $k_{m,n} = \mu/2$, and $k_{m,n} < \mu/2$. The solutions are obtained by solving the homogeneous equation using the initial conditions

$$T_{m,n}(0) = 0 \quad (42)$$

$$T_{m,n}(0) = c^2 f_{m,n} \quad (43)$$

For example, when $k_{m,n} > \mu/2$

$$T_{m,n}(t) = c^2 f_{m,n} \frac{\sin(\omega_{m,n} t) e^{-t/(\theta)}}{\omega_{m,n}} \quad (44)$$

where

$$\omega_{m,n} = c \sqrt{k_{m,n}^2 - \left(\frac{\mu}{2}\right)^2} \quad ; \quad (45)$$

the other cases have similar solutions involving a first-order polynomial of t or \sinh instead of sine.

Finally, the force was assumed to be an upward-directed impulse uniformly distributed (Figure B-2) over the central quarter of the groundplane for which $L_x/4 \leq x \leq 3L_x/4$ and $L_y/4 \leq y < 3L_y/4$. This allows the coefficients $f_{m,n}$ to be calculated.

This mathematical apparatus describes an impulsive deformation, as shown in Figure 3, which is a series of "snapshots" of the deformation from the instant the impulse occurs until after the spreading deformation wave reflects off the edge of the groundplane (a mass discontinuity) and again converges toward the center of the groundplane.

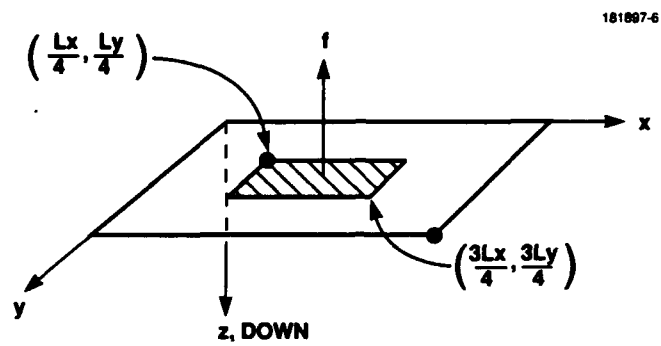


Figure B-2. Schematic drawing of radar antenna groundplane (membrane) showing area (crosshatched) of applied impulse.

APPENDIX C MULTILATERATION

Figure C-1 shows a canonical multilateration geometry and previously described elements of the system. The right-handed measurement coordinate system shown in the figure may be defined as follows: Sensor O is defined to be at the origin; A is defined to be on the x axis at an unknown distance from the origin O; B is defined to be in the first quadrant of the x,y plane; its coordinates (except $z = 0$, which is known by definition) are unknown. The coordinates of the reflector P are also required. Table C-1 summarizes this information.

181887-32

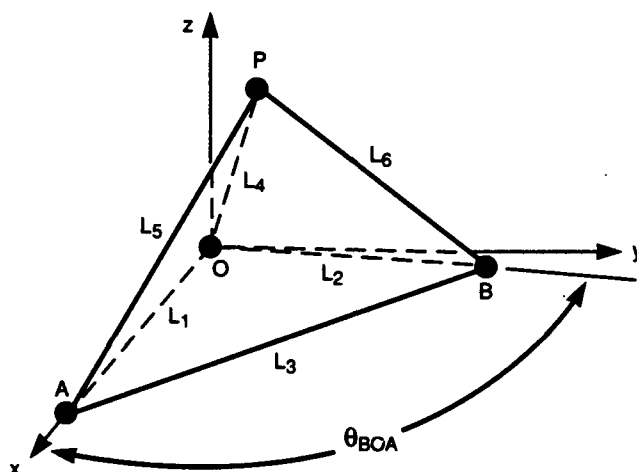


Figure C-1. Diagram showing multilateration geometry, including three sensors — A, B, and O — and the point P on the groundplane whose position is to be determined.

TABLE C-1
Unknown and Known Parameters of Points

Point	Coordinates*	Measurements **
A	$(x_A, 0, 0)$	l_1
B	$(x_B, y_B, 0)$	l_2, l_3
P	(x_C, y_C, z_C)	l_4, l_5, l_6
* These are unknown.		
** See Table C-2.		

Six measurements — the distances between the four system elements at the points of the pyramid, taking the points in pairs — are made. There are six unknowns, the coordinates x_A , x_B , y_B , x_P , y_P , and z_P of points A, B, and P, respectively. The coordinates may then be calculated (see Table C-2) from the measurements.

These formulas may be derived from the definitions by using elementary trigonometry (primarily the law of cosines).

By definition

$$x_A = l_1 \quad (46)$$

x_B may then be obtained by using the law of cosines.

$$x_B = (l_1^2 + l_2^2 - l_3^2) / (2l_1) = l_2 \cos(\theta_{BOA}) \quad (47)$$

As the vector that locates B has only two components, y_B may now be computed.

$$y_B = (l_2^2 - x_B^2)^{1/2} \quad (48)$$

TABLE C-2
Measurements Used for Multilateration

Measurement	Side of Pyramid
l_1	OA
l_2	OB
l_3	AB
l_4	OP
l_5	AP
l_6	BP

Finally, by using techniques similar to those described, the coordinates for the unknown point may be calculated.

$$x_P = (l_1^2 + l_4^2 - l_5^2) / (2l_1) \quad (49)$$

$$y_P = ((l_2^2 + l_4^2 - l_6^2) / 2 - x_P x_B) / y_B \quad (50)$$

as

$$x_P x_B + y_P y_B = l_2 l_4 \cos(\theta_{POB}) = (l_2^2 + l_4^2 - l_6^2) / 2 \quad (51)$$

and

$$z_P = (l_4^2 - x_P^2 - y_P^2)^{1/2} \quad (52)$$

Figure C-2 shows four reflectors, Q, C, D, and E, and the coordinate axes of the measurement coordinate system, u_x , u_y , and u_z , respectively. Suppose that it is necessary to set up a second, primed (antenna) right-handed coordinate system to be constructed as follows: Reflector Q is defined to be at the origin; C is defined to be on the x' axis at an unknown distance from the origin Q; D is defined to be in the first quadrant of the x', y' plane; its primed coordinates (except $z' = 0$, which is known by definition) are unknown.

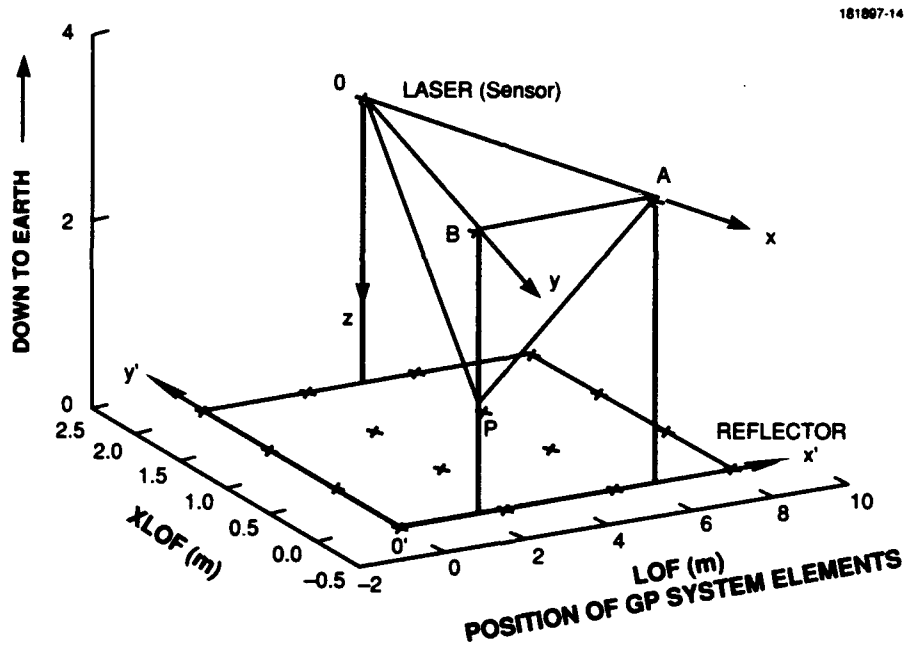


Figure C-2. Typical groundplane-measurement-system layout.

Using these definitions, one may write equations for the x' , y' , and z' coordinate system unit vectors, \underline{v}_x , \underline{v}_y , and \underline{v}_z , as resolved in the measurement coordinate system:

$$\begin{aligned}\underline{v}_x &= (\underline{r}_C - \underline{r}_Q) |\underline{r}_C - \underline{r}_Q|^{-1/2} \\ \underline{v}_y &= (1 - \underline{v}_x^T \underline{v}_x^T) (\underline{r}_D - \underline{r}_Q) \{1 - [\underline{v}_x^T (\underline{r}_D - \underline{r}_Q)]^2\}^{-1/2} \\ \underline{v}_z &= \underline{v}_x \times \underline{v}_y\end{aligned}\quad (53)$$

where $|\underline{r}|$ is the magnitude of the vector \underline{r} , $\underline{r}_i^T = [x_i, y_i, z_i]$ is the vector that locates point $i = Q, C, D$, or E in the measurement coordinate system, and \times is the vector (cross) product.

Also, it is necessary to calculate the primed coordinates of reflector E , whose coordinates are unknown. The coordinates of point E in the primed, or antenna, system will be the components of the column vector obtained by evaluating this equation:

$$\underline{r}_E' = \begin{bmatrix} \underline{v}_x^T \\ \underline{v}_y^T \\ \underline{v}_z^T \end{bmatrix} (\underline{r}_E - \underline{r}_Q) \quad (54)$$

APPENDIX D LEAST SQUARES

Elsewhere in this report, the following equation was derived for the deformations $z_{m,n}(x,y,t)$ of the model antenna's groundplane:

$$z_{m,n}(x,y,t) = T_{m,n}(t) \cos(\pi nx / L_x) \cos(\pi ny / L_y) \quad (55)$$

This is expressed in the coordinate system of the undeformed antenna, which is not that of the measurement system. The undeformed antenna-coordinate system is fictitious; measurements cannot be transformed into it. Measurements can only be transformed into an appropriately defined instantaneous antenna coordinate system. The transformation between two coordinate systems was derived in Appendix B.

It is possible to avoid transforming from one coordinate system to another before performing a least-squares fit by assuming that the antenna has certain geometrical properties, expressing these properties in terms of unknown constants, then determining these constants via the least-squares procedure.

Assume that the deformations $z_{m,n}$ are relative to a fictitious plane that is both rotated and translated relative to the measurement-coordinate system; therefore, a vector \underline{r}_i that locates the i th point on the deformed groundplane has the form

$$\underline{r}_i = R (\underline{x}_i + \sum_{m,n}^{m \text{ MAX } n \text{ MAX}} z_{m,n} \underline{u}_z) + \underline{l} \quad (56)$$

where \underline{u}_z is the z unit vector $[0,0,1]^T$ and $\underline{x}_i = [x_i, y_i, 0]^T$ is a vector whose elements are the coordinates of the undeformed point, and \underline{l} is an unknown constant vector.

Further, the rotations that R represents will generally be a small tilt (rotation through angles ϕ_x or ϕ_y , respectively) about the x and y axes followed by a (possibly) sizable rotation (through angle θ) about the z axes. The general form for R may be written as follows:

$$R = \begin{bmatrix} C & +S & \phi_x S - C \phi_y \\ -S & C & S \phi_y + C \phi_x \\ \phi_y & -\phi_x & 1 \end{bmatrix} \quad ; \quad (57)$$

$C = \cos(\theta)$ and $S = \sin(\theta)$.

The z component Δz_i of deformed location \underline{r}_i has the largest contribution from $z_{m,n}$, so it is used for determining the mode amplitudes.

$$\begin{aligned}\Delta z_i &= [0, 0, 1] \underline{z}_i \\ \Delta z_i &= \phi_y x_i - \phi_x y_i + L_z + \sum_{mn}^{m_{\text{MAX}} n_{\text{MAX}}} z_{m,n} \\ &= \underline{h}_i^T \underline{x} \quad ,\end{aligned}\tag{58}$$

where these definitions apply:

$$\begin{aligned}\psi_{m,n,i} &\triangleq \cos(\pi n x_i / L_x) \cos(\pi m y_i / L_y) \\ \underline{h}_i^T &\triangleq [1, x_i, y_i, \psi_{0,1}, \dots, \psi_{1,0}, \dots, \psi_{2,0}, \dots, \psi_{m_{\text{MAX}}, n_{\text{MAX}}}] \quad ,\end{aligned}\tag{59}$$

and

$$\underline{x} \triangleq [\beta, +\phi_y, -\phi_x, T_{0,1}, \dots, T_{1,0}, \dots, T_{2,0}, \dots, T_{m_{\text{MAX}}, n_{\text{MAX}}}] \quad ,\tag{60}$$

with

$$\beta \triangleq (l_z + T_{0,0}) \quad .\tag{61}$$

Note that two indistinguishable constants have been combined into β .

Then one may finally write the equation relating measurements Δz_i and unknowns \underline{x} (to be determined) via the least-squares procedure:

$$\underline{\Delta z} = \mathbf{H} \underline{x} \quad .\tag{62}$$

Standard methods may then be used to obtain the usual equation for the optimum \underline{x} , $\underline{x}_{\text{OPT}}$.

$$\underline{x}_{\text{OPT}} = (\mathbf{H}^T \mathbf{H})^{-1} \mathbf{H}^T \underline{\Delta z} \quad ,\tag{63}$$

where

$$\underline{\Delta z} = \begin{bmatrix} \Delta z_1 \\ \Delta z_2 \\ \vdots \\ \Delta z_M \end{bmatrix} \quad , \quad \mathbf{H} = \begin{bmatrix} \underline{h}_1^T \\ \underline{h}_2^T \\ \vdots \\ \underline{h}_M^T \end{bmatrix} \quad ,\tag{64}$$

and M (= 64 or 121) measurements are used to obtain \underline{x} .

REFERENCES

1. R.W. Miller (memo, 1988).
2. E. Hesham Attia, "Self-cohering airborne distributed array," Rome Air Development Center, Griffiss AFB, NY, RADC-TR-88-109 (June 1988). DTIC AD-198783.
3. B.D. Steinberg, "Radar imaging from a distorted array: the radio camera algorithm and experiments," *IEEE Trans. Ant. and Prop.* AP-29, No. 5, 740-748 (1981).
4. B. Kang, H.M. Subram, and B.D. Steinberg, "Improved adaptive-beamforming target for self-calibrating a distorted phased array," *IEEE Ant. and Prop.* 38, No. 2, 186-193 (1990).
5. E. Hesham Attia and B.D. Steinberg, "Self-cohering large antenna arrays using the spatial correlation properties of radar clutter," *IEEE Ant. and Prop.* 37, No. 1, 30-38 (1989).
6. E-A. Lee and C.N. Dorny, "A broadcast reference technique for self-cohering of large antenna phased arrays," *IEEE Trans. Ant. Prop.* 37, No. 8, 1003-1010 (1989).
7. A.J. Fenn and E. Kelly, private communication (20 September 1989)
8. E.J. Kelly, private communication (December 1983).
9. D.G. Zimcik, "Mechanical performance of the Radarsat SAR antenna," *Canadian Aeronautics and Space Journal* 35, No. 1 (1989).
10. R.W. Miller, private communication (27 November 1987).
11. G.J. Sonnenberg, *Radar and Electronic Navigation*, 6th ed., London: Butterworths, Chapter 7 (1988).
12. E.A. Swanson and G.H. Walther, "New laser sources," Division 6 seminar (5 February 1991).
13. A. Slotwinsky (Digital Signal Corporation), submitted paper, NASA Technology Workshop on Earth Science Geostationary Platforms (21-22 September 1989).
14. R.W. Miller, unpublished.
15. R.A. Becker, *Introduction to Theoretical Mechanics*, New York, NY: McGraw-Hill (1954).
16. A. Gray and G.B. Mathews, *A Treatise on Bessel Functions*, New York, NY: Dover Publications, Inc. (1966).

REPORT DOCUMENTATION PAGE

Form Approved
OMB No. 0704-0188

Public reporting burden for this collection of information is estimated to average 1 hour per response, including the time for reviewing instructions, searching existing data sources, gathering and maintaining the data needed, and completing and reviewing the collection of information. Send comments regarding this burden estimate or any other aspect of this collection of information, including suggestions for reducing this burden, to Washington Headquarters Services, Directorate for Information Operations and Reports, 1215 Jefferson Davis Highway, Suite 1204, Arlington, VA 22202-4302, and to the Office of Management and Budget, Paperwork Reduction Project (0704-0188), Washington, DC 20503.

1. AGENCY USE ONLY (Leave blank)		2. REPORT DATE 5 November 1991	3. REPORT TYPE AND DATES COVERED Technical Report	
4. TITLE AND SUBTITLE Compensating for Groundplane Deformations of a Space-Based Radar to Improve Clutter Cancellation Performance			5. FUNDING NUMBERS C — F19628-90-C-0002 PR — 227 PE — 63250F	
6. AUTHOR(S) George H. Emmons				
7. PERFORMING ORGANIZATION NAME(S) AND ADDRESS(ES) Lincoln Laboratory, MIT P.O. Box 73 Lexington, MA 02173-9108			8. PERFORMING ORGANIZATION REPORT NUMBER TR-931	
9. SPONSORING/MONITORING AGENCY NAME(S) AND ADDRESS(ES) U.S. Air Force Electronic Systems Division Hanscom AFB, MA 01730			10. SPONSORING/MONITORING AGENCY REPORT NUMBER ESD-TR-91-110	
11. SUPPLEMENTARY NOTES None				
12a. DISTRIBUTION/AVAILABILITY STATEMENT Approved for public release; distribution is unlimited.			12b. DISTRIBUTION CODE	
13. ABSTRACT (Maximum 200 words) Effects of deformations on the clutter cancellation of a hypothetical large phased-array space-based radar antenna groundplane are described. The radar is assumed to use a displaced-phase-center antenna (DPCA) for cancelling stationary ground clutter. A multilateration method of measuring the deformations is analyzed to determine its effectiveness in compensating for the deformations and improving clutter cancellation. Finally, a data staleness problem inherent in the proposed serial sampling method is described, a potential solution is presented, and its feasibility is discussed.				
14. SUBJECT TERMS radar antenna deformation displaced phase center antenna deformed antenna phase compensation radar antenna deformation measurements			15. NUMBER OF PAGES 74 16. PRICE CODE	
17. SECURITY CLASSIFICATION OF REPORT Unclassified	18. SECURITY CLASSIFICATION OF THIS PAGE Unclassified	19. SECURITY CLASSIFICATION OF ABSTRACT Unclassified	20. LIMITATION OF ABSTRACT SAR	